Engineering Structures 352 (2026) 122103

Contents lists available at ScienceDirect

Engineering Structures

journal homepage: www.elsevier.com/locate/engstruct

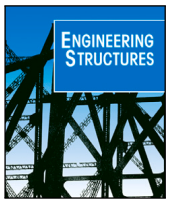

# Identification of mechanism-specific persistent scatterers for enhancing MT-InSAR in Structural Health Monitoring applications☆

Hao Kuai [a,*], Valentina Macchiarulo [a,b], Satyadhrik Sharma [a,c], Pantelis Karamitopoulos [d], Francesco Messali [a], Alice Cicirello [e], Giorgia Giardina [a]

[a] Delft University of Technology, 2628 CN, The Netherlands
[b] ARGANS Ltd, PL6 8BX, United Kingdom
[c] Netherlands Organisation for Applied Scientific Research (TNO), 2629 JD, The Netherlands
[d] City of Amsterdam, 1011 PN, The Netherlands
[e] University of Cambridge, CB2 1PZ, United Kingdom

ARTICLE INFO

*Keywords:*
Structural Health Monitoring
Remote sensing
Persistent scatterers
Surface deformation reconstruction error
Uncertainty quantification
Infrastructure

ABSTRACT

Growing incidents of structural damage and failures underscore the urgent need for more advanced Structural Health Monitoring (SHM) solutions. While Multi-Temporal Interferometric Synthetic Aperture Radar (MT-InSAR) has revolutionised SHM by enabling automated, long-term, and large-scale displacement monitoring of structures using Persistent Scatterers (PSs), its applicability is often constrained by the unpredictable spatial distribution of PSs. Conventional suitability assessments that rely primarily on PS density fail to account for the underlying structural behaviours, limiting their reliability.

This paper introduces a novel structural-based inverse approach that uniquely integrates MT-InSAR characteristics with structural response modelling to overcome these limitations. Unlike existing approaches, the method explicitly evaluates whether observed surface displacements adequately represent a target damage mechanism by comparing outputs from a pseudo sensor with those from a virtual MT-InSAR sensor. If this condition is satisfied, it then determines the minimum required number and optimal spatial arrangement of ideal PSs using modified pivoted QR factorisation, where satellite-induced positional uncertainties are rigorously modelled through Radial Basis Function kernels.

The proposed method was validated on a quay wall in Amsterdam using Finite Element Method (FEM) simulations of three distinct damage mechanisms. Results demonstrate its unique capability to quantitatively assess displacement representativeness and to pinpoint ideal PSs for robust monitoring. Leveraging these insights, the method was further applied to evaluate MT-InSAR monitoring feasibility across Amsterdam's historic centre, successfully identifying quay wall segments amenable to reliable observation. This work represents a significant advancement in MT-InSAR-based SHM, providing a more targeted and structurally informed approach for real-world infrastructure monitoring.

## 1. Introduction

A significant portion of the world's infrastructure was constructed decades ago and no longer meets modern service demands or does not comply with current standards and regulations [1–3]. At the same time, the increasing frequency and intensity of environmental stressors pose growing risks to these ageing structures, accelerating their degradation [4,5]. Consequently, regular infrastructure monitoring has become a global priority [6,7].

In response, several countries have developed formal monitoring guidelines, such as the U.S. National Bridge Inspection Standards (NBIS) [8,9], China National Standards for Technical Condition Evaluation of Highway Bridges [10], Italian National Standard [11], and German National Standard [12]. Although these guidelines have been periodically revised, they continue to rely heavily on visual inspections and non-destructive testing methods. While effective in engineering practice, these techniques are labour-intensive and costly, limiting their scalability and frequency of application [13,14]. Furthermore,

☆ This article is part of a Special issue entitled: 'Smart Sensing for SHM' published in Engineering Structures.

* Corresponding author.
*E-mail address:* h.kuai@tudelft.nl (H. Kuai).

https://doi.org/10.1016/j.engstruct.2026.122103

compliance with the prescribed regular inspection intervals does not always guarantee structural safety [15].

### 1.1. MT-InSAR as a promising alternative for SHM

Multi-Temporal Interferometric Synthetic Aperture Radar (MT-InSAR) has emerged as a promising alternative to traditional Structural Health Monitoring (SHM) methods. By processing a series of satellite images over time, MT-InSAR provides displacement data for infrastructure monitoring [16] using Persistent Scatterers with stable backscattering properties that enable millimetre level accuracy [17–19]. Unlike conventional SHM methods, MT-InSAR does not require in-situ sensor installation, is less labour-intensive, and functions under all lighting conditions. Satellite revisit intervals can be as short as a few days, enabling frequent and spatially extensive monitoring.

Numerous studies have demonstrated MT-InSAR's ability to detect structural anomalies across various types of infrastructure, including bridges [20–23], tunnels [24–26], buildings [27–29], dams [30–32], and railways [33–36]. These anomalies, typically identified through unusual displacement patterns in PSs located on structures, can serve as early warning signs of damage [37]. Therefore, both the quantity and spatial distribution of PSs are crucial to MT-InSAR's effectiveness. However, identifying PSs on a given structure is subject to uncertainty, as it depends on both the quality and temporal stability of radar backscatter, which are influenced by surface characteristics, weather conditions, sensor resolution, acquisition geometry, and the nature of deformation [38–40]. These factors affect not only the number of PSs but also their spatial distribution, ultimately influencing MT-InSAR's reliability for SHM.

### 1.2. Limitations of existing evaluation approaches

Despite its promise, there is currently no standardised approach for evaluating whether the spatial distribution and number of PSs obtained through MT-InSAR for a given structure are sufficient for effective SHM. Most studies assume that a sufficient number or density of PSs guarantees reliable monitoring [41–46]. While this approach has yielded promising results, it suffers from three main limitations. First, while MT-InSAR detects PSs only on a structure's surface, some structural behaviours do not manifest as surface displacements, meaning that even a high PS density may fail to capture relevant structural behaviour. Second, although PS density is commonly used as a proxy for effectiveness, no threshold has been proposed to define when MT-InSAR becomes a viable SHM method. Finally, PS density metrics typically ignore structural information such as geometry, loading conditions, and the nature of potential mechanisms, which can influence the displacement field. For instance, a simple, undamaged beam bridge under uniform loading may require only a few PSs to capture its half-sine deflection profile. In contrast, a more complex structure subjected to localised damage would require a different PS distribution. Solely relying on PS density risks underestimating or misrepresenting MT-InSAR's actual potential.

### 1.3. Introducing the concept of ideal PSs

To overcome these limitations, we propose shifting the focus from PS density to the concept of "ideal PSs", which refer to the minimal set of optimally located PSs required to fully capture a structure's displacement behaviour. These ideal PSs serve as a benchmark to evaluate the adequacy of real PSs detected by MT-InSAR. If the observed PSs spatially cover the ideal set, MT-InSAR can be considered suitable for SHM in that structure. If not, its use may be inadequate.

Identifying ideal PSs, in terms of both quantity and locations, can be achieved using pivoted QR factorisation [47], a method proven effective for sparse sensor placement in fields such as fluid dynamics and ocean monitoring [48,49]. This technique ranks points in the structure based on their importance in reconstructing the full displacement field. Additionally, pivoted QR factorisation is computationally efficient while maintaining accuracy [48], allowing scalable analysis across multiple infrastructures.

However, applying pivoted QR factorisation to MT-InSAR-based SHM presents unique challenges. First, unlike traditional sensor systems, MT-InSAR can only measure displacements at surface-accessible PSs. Therefore, before identifying ideal PSs, we must determine whether surface displacements adequately represent the internal structural behaviour. Second, the PS detection process is subject to position uncertainty [50,51], which must be accounted for in evaluating MT-InSAR's capability.

### 1.4. A structural-based inverse approach for evaluating MT-InSAR

Building on the concept of "ideal PSs", we propose a structural-based inverse approach to evaluate MT-InSAR's suitability for SHM. This approach incorporates both the physical characteristics of the structure and the position uncertainties associated with MT-InSAR measurements. The potential evaluation bias caused by measurement noise is also discussed. The process starts with a numerical simulation of the target structure, including potential damage mechanisms. Displacement data from the simulation are then analysed to assess whether surface displacements alone can capture the complete structural response. If so, ideal PSs are identified using a modified pivoted QR factorisation approach, which incorporates a kernel function to account for PS position uncertainties from MT-InSAR. This approach offers a comprehensive and scalable evaluation of MT-InSAR's effectiveness for infrastructure monitoring.

We applied the proposed approach to the Marnixkade quay wall in Amsterdam. Three damage mechanisms were simulated: failure due to traffic loading, degradation of central foundation piles, and degradation of randomly distributed foundation piles. For each case, we evaluated whether surface displacements could reliably represent internal behaviour, and subsequently identified the corresponding ideal PSs.

To further demonstrate its practical application, the identified ideal PSs were used as benchmarks to assess MT-InSAR's effectiveness across all quay walls in the historic centre of Amsterdam, assuming that these structures exhibit similar behaviour to the Marnixkade quay wall. Real PS data were collected in both ascending and descending satellite tracks from 2011 to 2020. By comparing the spatial distribution of the observed PSs with the ideal PS benchmarks, we evaluated the monitoring coverage and reliability. This application illustrated how the proposed approach can support a systematic evaluation of MT-InSAR's suitability for SHM and provides a clear path for its integration into operational monitoring frameworks.

## 2. Methodology

This paper proposes a structural-based inverse approach to evaluate the feasibility of applying MT-InSAR for SHM. As shown in Fig. 1a, when MT-InSAR is employed to monitor infrastructure, it uses PSs positioned on the structure surface to measure displacements over time. If PSs are sufficient in number and well-distributed, their displacements can effectively reflect the structural deformation patterns. Since these patterns vary depending on the type of structural damage mechanism that is observed, they may offer insights into the location, severity, and nature of structural damage.

To determine whether MT-InSAR can effectively detect specific structural damage mechanisms, we proposed a methodology that reversed the conventional monitoring process (Fig. 1b). This inverse approach consists of four steps: (i) generating a displacement basis matrix through numerical simulations of relevant structural damage mechanisms, (ii) evaluating the representativeness of surface displacements by comparing reconstruction errors between pseudo sensor and virtual MT-InSAR, (iii) identifying ideal PSs using modified pivoted QR factorisation, and (iv) integrating PS position uncertainties into ideal PS regions. Each step is outlined in detail below.

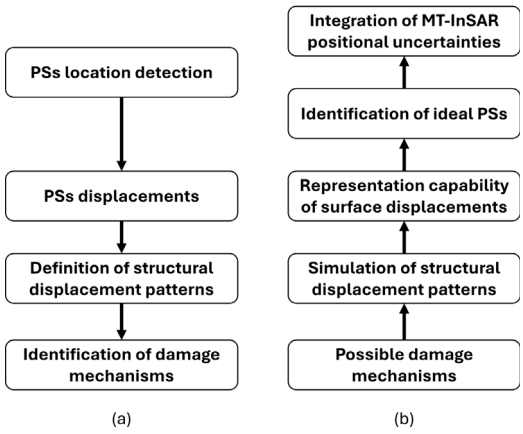


**Fig. 1.** MT-InSAR monitoring (a) and structural-based inverse evaluation (b) for SHM.

### 2.1. Displacement basis matrix generation

The structural-based inverse approach began by identifying potential damage mechanisms that a structure might experience. These were categorised into two types: acute mechanisms, which occurred suddenly, e.g., due to extreme loads or impact, and progressive mechanisms, which evolved gradually over time. Due to the temporal resolution of MT-InSAR measurements, the technology is inherently better suited for monitoring progressive mechanisms rather than acute ones, which may occur too rapidly to be captured between satellite acquisitions. Consequently, this study focused exclusively on progressive damage mechanisms.

For each progressive mechanism identified, a displacement basis matrix was generated using high-fidelity numerical simulations of the infrastructure under investigation and the relevant mechanism. Specifically, Finite Element (FE) models were developed, due to the FE method versatility and accuracy in modelling both linear and nonlinear structural behaviour. Depending on the structural typology and complexity of resulting damage, alternative methods such as the Discrete Element Method may also be applicable [52].

The output of these simulations was a state-space observation matrix $\mathbf{X}$, defined as:

$$\mathbf{X} = [\mathbf{x}_1, \mathbf{x}_2, \mathbf{x}_3, \mathbf{x}_4, \dots, \mathbf{x}_m] \tag{1}$$

Each column vector $\mathbf{x}_i$ represents the structure's displacement at time instant $i$, with $m$ total steps covering the full damage progression over time. Each row corresponds to the displacement time history of a single node. Dimensionality reduction techniques can be applied to $\mathbf{X}$ to extract the dominant spatial deformation modes, resulting in a reduced basis matrix $\mathbf{\Psi}$. One example is Proper Orthogonal Decomposition (POD), which extracts an orthogonal basis capturing the dominant spatial modes of the displacements [53].

### 2.2. Surface representation evaluation

Since MT-InSAR can only measure surface displacements, it is crucial to assess whether surface measurements alone can adequately reflect the global structural behaviour. To this end, two conceptual sensing models were introduced: pseudo sensor and virtual MT-InSAR (Fig. 2). The pseudo sensor assumed full access to all nodal displacements across the structure, representing an idealised extension of MT-InSAR and serving as a theoretical benchmark for comparison. The virtual MT-InSAR mimicked MT-InSAR constraints by restricting access to surface-visible nodes only.

For both models, the pivoted QR factorisation method, originally introduced by Businger and Golub [47] to solve least squares problems, was used to rank candidate observation points. This algorithm has demonstrated its effectiveness in various applications. However, it has never been applied to the selection of ideal PSs for MT-InSAR.

MT-InSAR surface measurements at $r$ selected PS points can be described mathematically as:

$$\mathbf{y} = \mathbf{C}\mathbf{x} \tag{2}$$

where $\mathbf{C} \in \mathfrak{R}^{r \times n}$ is the matrix encoding the positions of the PSs. The matrix $\mathbf{C}$ is usually populated by zeros and ones to identify individual components of $\mathbf{x}$. In the context of determining the ideal PSs, this matrix $\mathbf{C}$ is unknown, and the task is to identify the smallest number of PSs needed to capture the structural behaviour so that $r \ll n$.

Since the displacement pattern $\mathbf{x}$ corresponds to a particular instant in the evolution of a specific structural damage mechanism that can be observed through surface displacements, it can be assumed that the state $\mathbf{x}$ evolves in time according to a unknown nonlinear functional form $f$, so that $\dot{\mathbf{x}} = f(\mathbf{x}(t))$. Following [48], the dynamics can be expressed on a low-dimensional space obtained by identifying an appropriate transformation basis $\mathbf{\Psi}$ that reduces the number of active components:

$$\mathbf{x} = \mathbf{\Psi}\mathbf{s} \tag{3}$$

where $\mathbf{s}$ is a sparse vector of coefficients that identifies the active spatial eigenmodes collected in the matrix $\mathbf{\Psi}$ (note: mode here does not refer to the structural modes of the underlying structure). Since this is a time-evolving problem, the coefficients $\mathbf{s}$ are time-dependent. This means that instead of collecting high-dimensional states $\mathbf{x}$, we aim to compress and discard most of the information by inferring the $\mathbf{s}$ in the transformed coordinate system.

By combining Eqs. (2) and (3), the problem can be reformulated as:

$$\mathbf{y} = \mathbf{C}\mathbf{x} = \mathbf{C}\mathbf{\Psi}\mathbf{s} = \mathbf{\Theta}\mathbf{s} \tag{4}$$

When using MT-InSAR to collect the displacement of PSs, $\mathbf{C}$ and $\mathbf{y}$ are obtained after the MT-InSAR analysis. Ideally, the sparse vector $\mathbf{s}$ can then be obtained using the Moore–Penrose pseudoinverse [54].

$$\mathbf{s} = (\mathbf{C}\mathbf{\Psi})^{\dagger}\mathbf{y} \tag{5}$$

In our study, identifying the ideal PSs involved selecting an effective measurement matrix $\mathbf{C}^*$ that contained only ones at the locations of the ideal PSs, such that the displacement data $\mathbf{y}$ collected at these points could be used to derive the sparse vector $\mathbf{s}$ via Eq. (5) with high accuracy. Numerically, this involved designing $\mathbf{C}^*$ such that $\mathbf{\Theta}$ was well conditioned. A well-conditioned $\mathbf{\Theta}$ reduced numerical instability during signal reconstruction and ensured reliable computation of $\mathbf{s}$. To achieve this, the pivoted QR factorisation was effectively used, as recommended by [48].

Matrices often contain sets of linearly dependent columns. Pivoted QR factorisation aims to identify a set of columns that are "as linearly independent as possible". The process iteratively selects one column at a time. At each step, it chooses the column that is most difficult to represent as a combination of the columns that have already been selected in the previous steps, using the norm to quantify this difficulty. In this context of this study, applying pivoted QR factorisation to the basis matrix $\mathbf{\Psi}$ for a potential damage mechanism produced the effective measurements matrix $\mathbf{C}^*$, identified by the pivot columns, along with an orthonormal matrix $\mathbf{Q}$ and an upper triangular matrix $\mathbf{R}$:

$$\mathbf{\Psi}^{\top}\mathbf{C}^{*\top} = \mathbf{Q}\mathbf{R} \tag{6}$$

Specifically, the pivoted QR factorisation processed the basis matrix $\mathbf{\Psi}^{\top}$ and obtained the ideal PSs matrix $\mathbf{C}^*$ following the procedure as shown in Fig. 3. First, the column with the largest norm was selected from the matrix. This column corresponded to the first ideal PS and was moved to the first position in the matrix. Next, all the remaining

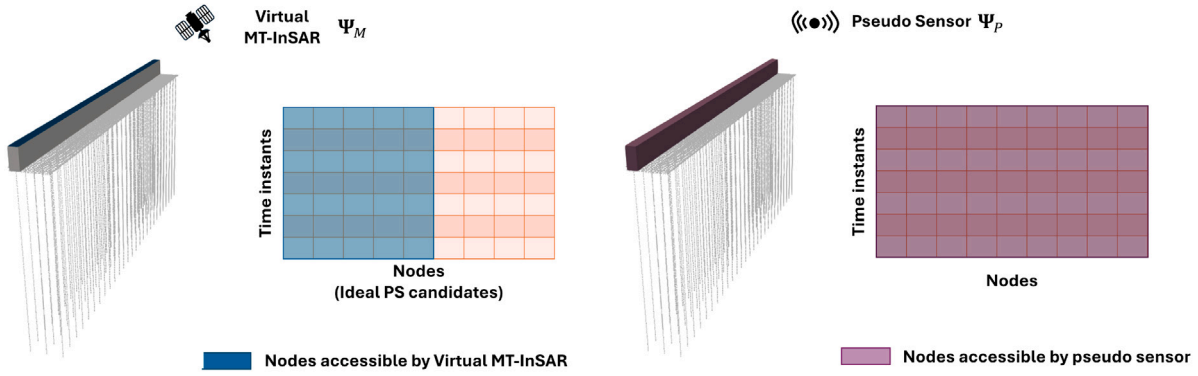


**Fig. 2.** Conceptual sensing models and their observation matrices: virtual MT-InSAR (left), which observes only the top surface of the structure; pseudo sensor (right), which observes all points of the structure.

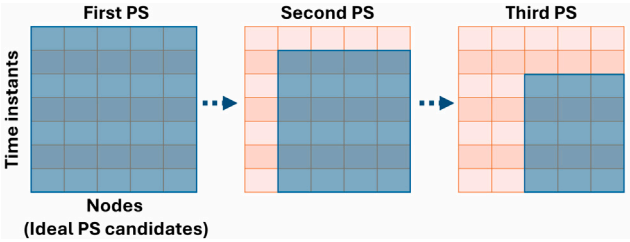


**Fig. 3.** Pivoted QR factorisation for structural-based inverse approach.

columns were orthogonalised with respect to this selected column. After orthogonalisation, the norms of the remaining columns were recalculated, and the column with the largest updated norm was chosen as the second ideal PS. This process, selecting the column with the largest norm and orthogonalising the remaining columns, was repeated iteratively until all columns had been processed. Ultimately, each column of $\mathbf{C}^*$ represented one of the potential candidates (i.e., ideal PSs for virtual MT-InSAR and ideal sensor locations for the pseudo sensor) ranked by significance.

To address whether surface displacements could sufficiently represent the overall structural behaviour, we compared the ability of top-ranked ideal PSs and ideal sensor locations to reconstruct the displacement pattern. This reconstruction was achieved through a linear mapping approach. It derived the relationship $\mathbf{L}$ between the training signals (displacement data from the selected $r$ candidate observation points at $v$ time instants) and prediction signals (displacement data from the same point at a time instant $t$) by minimising the following optimisation problem:

$$\min_{\mathbf{R}} \|\mathbf{aL} - \mathbf{b}\|_2 \tag{7}$$

where $\mathbf{a} \in \Re^{r\times v}$ is the matrix of training signals, and $\mathbf{b} \in \Re^{r}$ is the vector of the prediction signals at a time instant $t$. This relationship $\mathbf{L}$ was then used to reconstruct the displacement pattern of the entire structure, $\mathbf{x}_L \in \Re^{n}$, at a time instant $t$ as:

$$\mathbf{x}_L = \mathbf{AL} \tag{8}$$

where $\mathbf{A} \in \Re^{n\times v}$ is the training signal, including the displacements of all $n$ points in the structure throughout $v$ time instants in the mechanism evolution process.

The reconstruction ability of selected candidate observation points only based on numerical simulation results, the difference between the reconstructed displacement pattern $\mathbf{x}_L$ and the simulated displacement pattern $\mathbf{x}$ was referred to as the reconstruction error:

$$\mathbf{e}_L = \left|\mathbf{x}_L - \mathbf{x}\right| \tag{9}$$

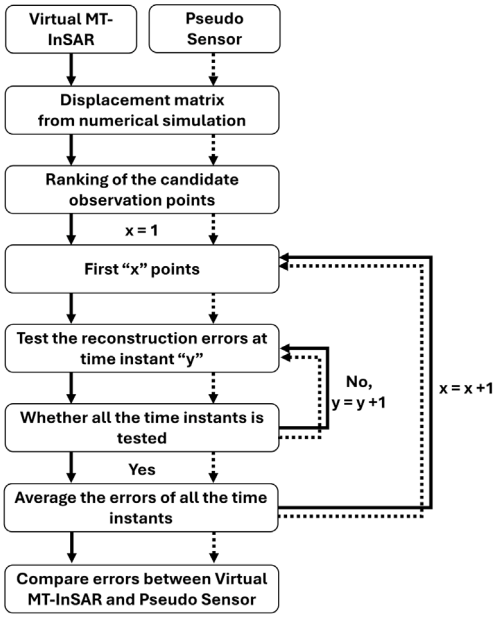


**Fig. 4.** The procedure of surface representation evaluation.

Two metrics were used to assess this ability: the Mean Reconstruction Error, which represents the average error across all points in the structure and providing an overall measure of performance, and the Maximum Reconstruction Error, which indicates the largest error among all points and is critical for identifying localised inaccuracies that could mislead damage assessments. The reconstruction errors were evaluated at each time instant of the mechanism evolution. This ensured accuracy across all stages of the process and avoided overlooking discrepancies at specific time instants.

Fig. 4 summarises the procedure of surface representation evaluation. Firstly, only the displacements of the surface visible to MT-InSAR (the blue region in Fig. 2) obtained from numerical simulation were processed using pivoted QR factorisation to rank ideal PSs candidates. The reconstruction errors were then calculated iteratively, starting with the top-ranked ideal PS, followed by the top two, the top three, and so on. The pseudo sensor followed a similar procedure, but it considered the displacements of all points in the structure (the purple region in Fig. 2). If the reconstruction errors of virtual MT-InSAR were significantly larger than those for the pseudo sensor, then MT-InSAR was judged unsuitable for detecting the damage mechanism of the target structure. Otherwise, it was considered applicable for this purpose.

### 2.3. Ideal PSs identification

The reconstruction errors provided an overall indication of the ability of MT-InSAR to determine whether displacement data collected from surfaces accessible by MT-InSAR could adequately represent the global damage mechanism of the target structure. However, even if surface displacement data could theoretically represent the structural damage mechanism, MT-InSAR might still fail to provide a sufficient number of PSs or might result in poorly distributed PSs. As a result, the displacements derived from these PSs could still be unable to capture the full extent of the mechanism. This highlights the necessity of identifying the number and positions of ideal PSs, which can serve as benchmarks to evaluate MT-InSAR's ability in each specific case.

As previously mentioned, pivoted QR factorisation processes the basis matrix of virtual MT-InSAR to rank potential ideal PS candidates based on their significance. However, determining the number and regions of ideal PSs still involves addressing two key issues.

First, the positions of ideal PSs should be defined as regions rather than exact points. From the perspective of MT-InSAR, placing PSs within structures introduces inherent position uncertainties [50,51]. Even after applying correction methods, position uncertainties related to satellite measurements persist [55]. Structurally, when an exact location for a PS is identified, there are possibilities that nearby points may exhibit similar displacement behaviour. Therefore, considering both MT-InSAR's intrinsic position uncertainties and structural behaviour, identifying regions for ideal PSs placement is more practical.

Second, a cutoff point is required to determine the number of ideal PSs needed, based on the ranking of potential candidates. Reconstruction errors provide a general guidance here [48]. For instance, if the reconstruction error reaches an acceptable level with three ideal PSs, it may suggest that three ideal PSs are sufficient. However, this remains a rough estimation. The number of ideal PSs should comprehensively capture the displacement behaviour of the entire structure. While reconstruction errors offer a threshold-based assessment, they do not guarantee that the selected PSs fully represent the structural behaviour. The error threshold is arbitrary, whether set at 1 mm or 0.1 mm, and may not truly reflect how well the PSs capture the displacement pattern.

To identify the ideal PS regions, we modified the pivoted QR factorisation as shown in Fig. 5. A "Detected" part was introduced into the matrix during the determination of each ideal PS. This modification happened at each stage of the column pivot selection. For instance, after the first location of the ideal PS was identified, the corresponding column was moved to the "Detected" part. This ensured that once a location was chosen, it was excluded from further iterations. The remaining columns were then processed to find additional possible locations for the same ideal PS. This iterative process continued until all columns in the "To Be Detected" part were processed, generating a ranking of possible positions for each ideal PS.

Once the position ranking of each ideal PS candidate was obtained, displacement correlations between the initially selected position and the following selected positions were tested. The goal was to ensure that all points in the identified region of the same ideal PS exhibited similar behaviour during damage evolution. The Radial Basis Function (RBF) kernel was employed to evaluate this correlation:

$$K(\mathbf{x},\mathbf{y}) = \exp(-\gamma\|\mathbf{x}-\mathbf{y}\|^2) \tag{10}$$

where $\mathbf{x} \in \Re^m$, $\mathbf{y} \in \Re^m$ represent the displacement columns of the initially selected position and the subsequently selected position, respectively. The scale parameter $\gamma$ was set to $1/m$, where $m$ is total number of steps covering the full damage progression, to ensure the stabilisation of the RBF kernel [56].

Positions with high correlations were grouped into the same region. By applying a predefined threshold to the correlation values, the regions of each ideal PS were determined. Furthermore, these correlations guided the determination of the number of ideal PSs required

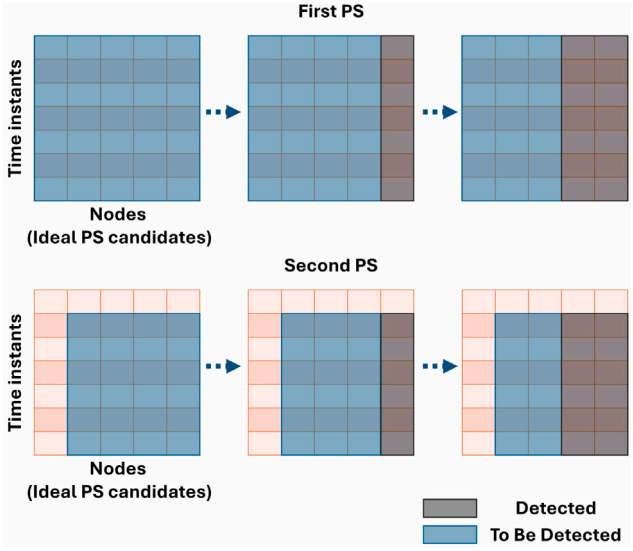


**Fig. 5.** Modified pivoted QR factorisation for identifying regions for PSs.

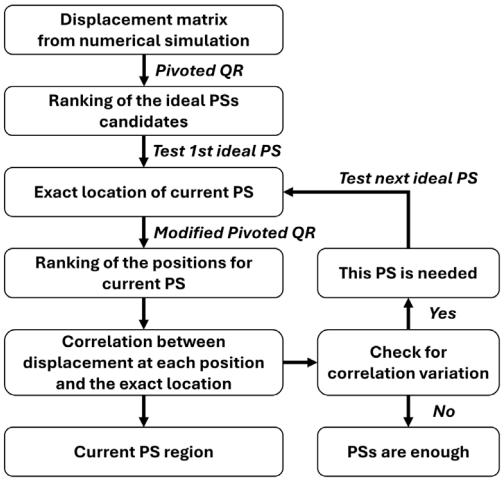


**Fig. 6.** The procedure of ideal PSs identification.

to comprehensively capture the target structural damage mechanism. If an ideal PS candidate exhibited consistently high correlations (close to 1) across all nodes on the structure, it implied that its contribution to capturing structural displacement behaviour is minimal, and this candidate could be excluded. If significant variations in correlation were observed, the candidate was considered essential. In this way, the correlation variation provides a data-driven and systematic cutoff for determining the number of ideal PSs, avoiding the subjectivity of a reconstruction-error threshold and ensuring that the full structural displacement behaviour is captured.

The entire procedure for determining the number and regions of ideal PSs is summarised in Fig. 6. Initially, the basic displacement matrix $\Psi_M$ was processed using pivoted QR factorisation to rank the ideal PS candidates. Each candidate was then analysed individually. The following process began by testing the first ideal PS. The modified pivoted QR factorisation was applied to rank the possible positions for this ideal PS. The displacement correlations between these positions and the initially selected position were then evaluated. If the correlation showed significant variation, this ideal PS was considered essential for capturing the structural behaviour; otherwise, it was regarded as unnecessary. The region of this PS was then defined by identifying positions whose correlations exceeded a predefined threshold. This

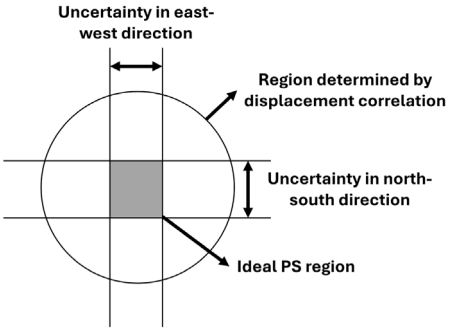


**Fig. 7.** Integration of MT-InSAR position-related uncertainties into ideal PS region identification.

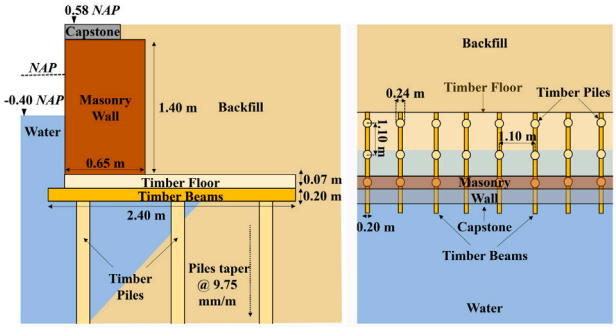


**Fig. 8.** The Marnixkade quay wall.
*Source:* (reproduced from [58,59])

procedure was repeated for the next ideal PS candidate until the correlation variation became sufficiently small, indicating that no additional PSs were needed.

### 2.4. Integration of PS position uncertainties

Up to this point, regions of ideal PSs have been determined based solely on numerical results of the structural displacement behaviour, specifically by assessing the similarity of displacement responses over time. While this approach ensured that selected PS regions were structurally representative, it did not account for position uncertainties inherent to MT-InSAR measurements, which can reach several metres, depending on the SAR sensor characteristics, orbital accuracy, and the geocoding process [57].

To address this, we introduced additional spatial constraints based on RBF kernels. These kernels characterised the spatial variability in measurement accuracy and were used to refine the previously identified PS regions, ensuring they lay within domains that MT-InSAR could reliably capture. Each directional uncertainty was represented by a dedicated RBF kernel. The scale parameter $\gamma$ captured the extent of the uncertainty in each direction:

$$\gamma = \frac{1}{\sigma^2} \tag{11}$$

where $\sigma^2$ represents the variance in the RBF kernel to model uncertainty in the respective direction.

By applying a predefined threshold to the kernel value in each direction, we defined uncertainty bounds accordingly. The ideal PS region was then defined as the intersection of the region derived from structural displacement correlations and the uncertainty bounds in two planar directions (east–west and north–south), as shown in Fig. 7. This ensured that the selected PSs are both structurally informative and practically measurable given MT-InSAR's spatial resolution and position-related uncertainties. In the vertical direction, the same predefined kernel threshold was mapped onto a tolerance band around the known structural surface, which was directly applied in the preliminary stage to filter the PS candidate, in line with standard practice [23]. For instance, considering the 2.22 m vertical uncertainty reported in the literature [55], we set $\sigma = 2.22$ in Eq. (11). The predefined correlation threshold of $K = 0.8$ was then mapped to a corresponding vertical tolerance of approximately 1.05 m. This tolerance was defined around the surface of the target structure and used to filter PS candidates in the preliminary stage.

### 2.5. Other uncertainty sources affecting the evaluation of MT-InSAR's effectiveness

In reality, the displacement measurements at real PS locations are affected by various sources of uncertainty [60]. Directly using the numerically simulated displacements neglects these uncertainties. Therefore, it is important to discuss how uncertainties could influence the displacement observations and how the estimation of MT-InSAR's effectiveness may be biased.

Typically, measurement uncertainty can be represented in terms of a random measurement noise (e.g., decorrelation noise) and/or systematic errors (e.g., orbital errors and topographic residuals) [40,60]. Since the random measurement noise is an aleatory irreducible uncertainty, while the systematic errors can be reduced if properly accounted for [61], in what follows only the random measurements noise is going to be considered. At each acquisition time, it can be assumed that the displacement from each PS is a statistically uncorrelated observation of the underlying true displacement. Given the limited information, it is reasonable to assume that these observations follow a Gaussian distribution. The measured displacement $\mathbf{A_{measure}}$ at real PSs can be expressed as:

$$\mathbf{A_{measure}} = \mathbf{A_{true}} + \epsilon,\ \epsilon \sim \mathcal{N}(0, \sigma^2_{\text{error}} I). \tag{12}$$

where $\mathbf{A_{true}}$ is the true displacement at real PS positions, which is not known, and $\epsilon$ represents an equivalent zero-mean measurement noise with variance $\sigma^2_{\text{error}}$.

Further, we assumed that the true displacement of the entire structure $\mathbf{A_{true}}$ can be obtained from simulations (i.e. the model has been validated and calibrated, and there are no sources of uncertainties [61] in the model form, model parameters or solver). Therefore, the error in reconstructing the displacements of the entire structure using ideal PS data $\mathbf{e}$ can be expressed as:

$$\mathbf{e} = \mathbf{x}_{L,\text{measured}} - \mathbf{x}_{L,\text{true}} = \mathbf{A_{measure}}\,\mathbf{L} - \mathbf{A_{true}}\,\mathbf{L} = \epsilon \cdot \mathbf{L} \tag{13}$$

where $\mathbf{x}_{\text{true}}$ is the true displacement of all the nodes in the structure, and $\mathbf{L}$ is the relationship calculated using Eq. (7). According to Eq. (13), the reconstruction will be affected proportionally to both the measurement noise level and the magnitude of the reconstruction coefficients. It is important to note that this noise impact is limited to the surface representation evaluation, where Eq. (8) is used.

## 3. Case study

To demonstrate the applicability of the proposed approach, this was applied to a historic quay wall located at Marnixkade in Amsterdam (see Fig. 8). Quay walls present particular monitoring challenges due to their limited top-surface area, which limits visibility in MT-InSAR data. Successfully identifying the number and location of ideal PSs under these constraints would highlight the method's potential for application to other types of infrastructure. The structural model used has been validated through both cross-model comparisons and field measurements, confirming its accuracy. Detailed description of the model and the finite element analysis can be found in [58,59].

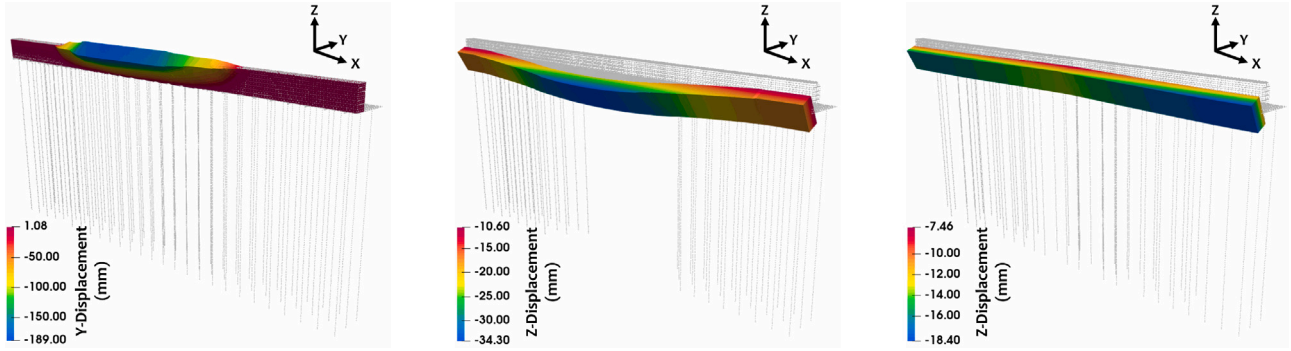


(a) Failure induced by traffic loading (Displacement scale factor: 10)

(b) Failure induced by central pile degradation (Displacement scale factor: 50)

(c) Failure induced by random pile degradation (Displacement scale factor: 50)

**Fig. 9.** Displacements and deformed configuration of the quay wall at the final load step. The dashed lines indicate the original, undeformed contour.

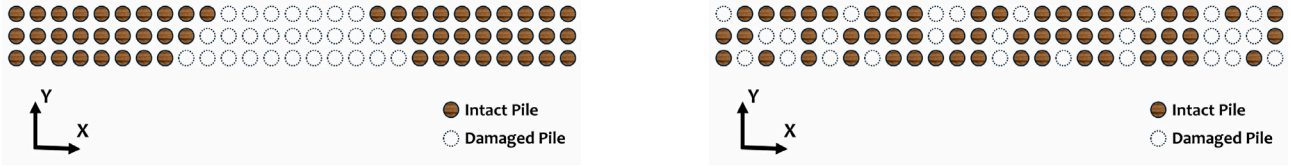


(a) Central pile degradation scenario

(b) Random pile degradation scenario

**Fig. 10.** Layouts of piles for different degradation scenarios.

### 3.1. Failure induced by traffic loading

The first mechanism was simulated by monotonically applying incremental lateral forces to the structure. These forces simulated the pressure induced by a truck positioned on the road, four metres from the quay wall. The vertical load from the truck weight was transferred through the soil and manifests as lateral pressure on the masonry wall and adjacent timber floor. The resulting structural response involved significant displacements at the top surface of the wall. The simulation captured the complete progression of damage up to failure over 110 load steps. Fig. 9(a) illustrates the lateral displacement of the quay wall at the end of the incremental load application.

### 3.2. Failure induced by degradation of central foundation piles

In the second scenario, failure was induced by the progressive degradation of a region of foundation piles located at the centre of the modelled section of the quay wall. This mechanism was based on inspection data from 2016, which identified deterioration in several central piles of the Marnixkade quay wall [62]. To simulate this, the cross-sectional diameters of 27 out of 81 piles were gradually reduced to zero, representing full structural failure (Fig. 10(a)). The simulation proceeded through 100 load steps, tracking the gradual collapse of the structure due to pile failure. Unlike the traffic loading case, this scenario produced primarily vertical displacements. Fig. 9(b) shows the vertical displacement field of the quay wall at the point of complete failure of the affected piles.

### 3.3. Failure induced by degradation of random foundation piles

While the two previous cases exhibited approximately symmetric deformation patterns, real-world scenarios are often non-symmetric. Additionally, the degradation of central piles is relatively rare in practice. To address these aspects, a third scenario was modelled in which 27 piles were randomly degraded, as shown in Fig. 10(b). The progression of this non-symmetric damage mechanism was simulated through 100 load steps, ultimately producing an irregular vertical displacement pattern across the quay wall surface. The final deformation state is shown in Fig. 9(c).

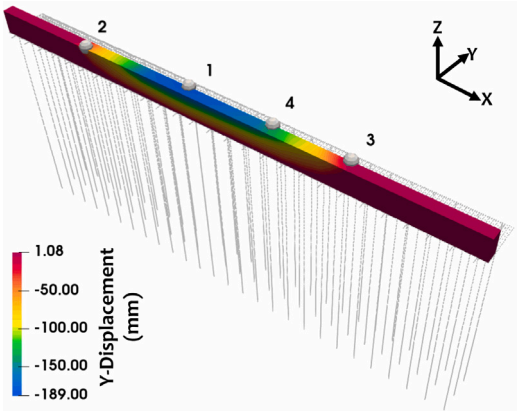


**Fig. 11.** Top selected ideal PSs and horizontal displacement at the final load step for the traffic loading failure case. All parts other than the masonry walls are shown in dashed lines.

## 4. Results

### 4.1. Failure induced by traffic loading

Fig. 11 shows the horizontal (Y-direction) displacements at the final load step of the numerical simulation. The results indicate that the application of a large and localised vertical load, such as the weight of a truck, induced large displacements at the central region of the wall (blue area), with maximum values reaching -189 mm. Since this structural damage mechanism primarily generated lateral displacements, the Y-direction displacements were the focus of the analysis.

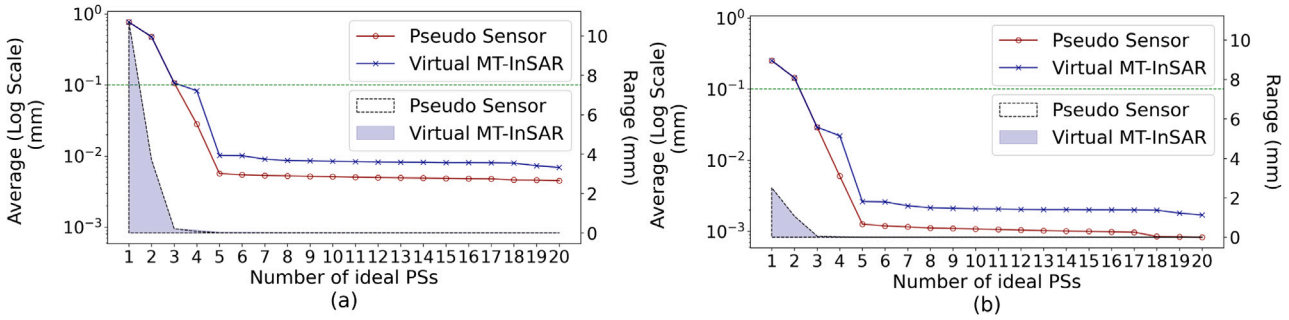


**Fig. 12.** Evaluation of the surface displacement capability to represent traffic loading failure: (a) maximum absolute reconstruction error and (b) mean square absolute reconstruction error. The average reconstruction error is shown by lines, while the dashed envelopes and the shaded areas represent the corresponding error ranges.

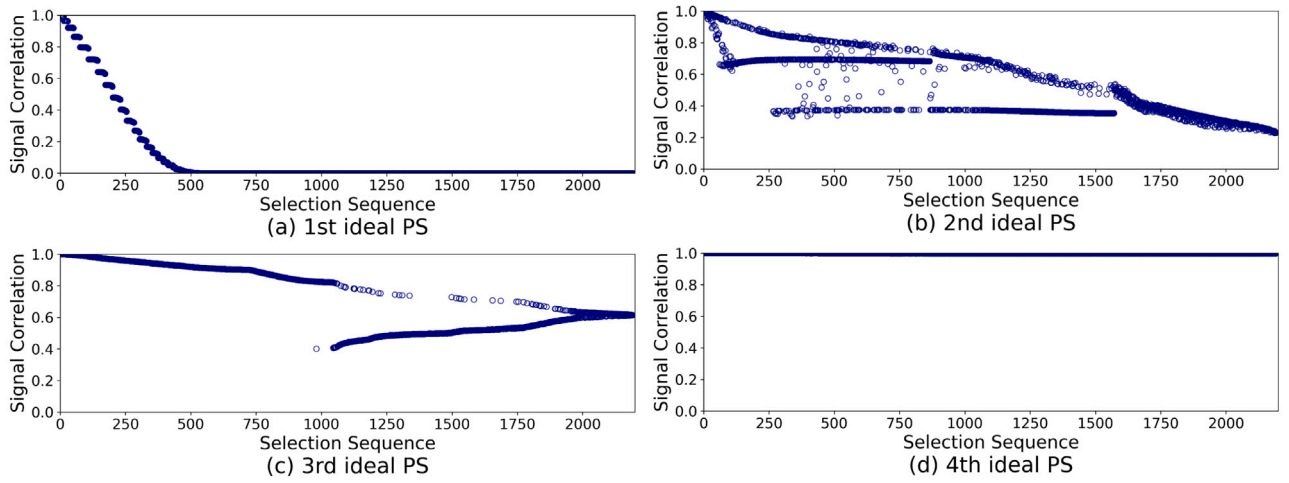


**Fig. 13.** Signal correlation trends during sequential selection for each ideal PS, in case of traffic loading failure.

First, we assessed whether displacement data acquired solely from the top surface were sufficient to represent the entire mechanism. To this end, we compared the reconstruction errors between the pseudo sensor and the virtual MT-InSAR data. For each load step, both the maximum absolute error and the mean square error were computed. To effectively summarise these results, Fig. 12 presents the average values across all load steps using red lines (pseudo sensor) and blue lines (virtual MT-InSAR) on a logarithmic scale. In addition, the full error range over all the load steps is visualised using a dashed envelope for the pseudo sensor and shaded areas for the virtual MT-InSAR. The results show that with only three ideal PSs, the virtual MT-InSAR achieves reconstruction accuracy that is comparable to the pseudo sensor, with average errors below 0.1 mm (indicated by the green dashed line). Furthermore, the error range is also well constrained from this point onward, indicating the robustness of surface measurements in capturing the full displacement behaviour. This suggests that top-surface monitoring using MT-InSAR may be sufficient to characterise the failure induced by traffic loading.

Then, pivoted QR factorisation was used to rank all surface points on the structure according to their suitability as ideal PSs. The top four ranked points are visualised as spheres in Fig. 11. The first point was located in the region exhibiting the largest displacement (blue area), capturing the peak deformation. The second and third points were positioned on either side of this central region, capturing the gradient between the severely and mildly affected areas (between red and yellow areas). The fourth point further refined the spatial distribution, lying between the maximum displacement region (blue area) and the moderate displacement region (green area). Overall, these four selected PSs were spatially well distributed and enabled representation of the entire mechanism, including both peak and transitional displacement regions.

Then, we determined the number of ideal PSs required and the corresponding regions they represented. To this end, a modified pivoted QR factorisation was applied for each top-ranked point. Unlike pivoted QR factorisation, the modified version sequentially selected surface points based on their ability to substitute for a given ideal PS. At each selection of an ideal PS, the displacement signal of the newly selected point was compared with that of the first selected point (the corresponding sphere in Fig. 11). Fig. 13 shows how the signal correlation evolves with the selection sequence for each of the top four ideal PSs. A clear downward trend in correlation values for the first three PSs (Fig. 13(a), (b), and (c)) indicates that the algorithm was effectively selecting points in order of decreasing representativeness. In contrast, the correlation values for the fourth ideal PS (Fig. 13(d)) remained consistently close to one throughout the selection process, suggesting that additional PSs beyond the third were redundant for accurately capturing the displacement characteristics.

To visualise these signal correlations spatially, the values were mapped onto the physical domain. For each ideal PS, the signal correlation of newly selected positions was represented by colour at their respective spatial locations. These colour maps are shown in the signal correlation panels of Figs. 14(a), 14(b), and 14(c). Positions with correlation values above 0.8 were considered to exhibit similar displacement behaviour and were regarded as viable alternatives to the selected PS from a signal similarity perspective (highlighted by black outlines in each panel).

Subsequently, positional uncertainties inherent in MT-InSAR were considered. These uncertainties depend on both the satellite and the

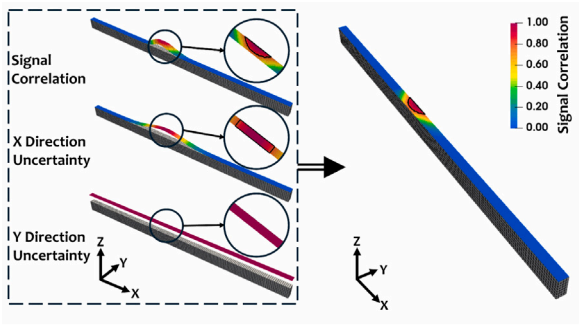


(a) First ideal PS region

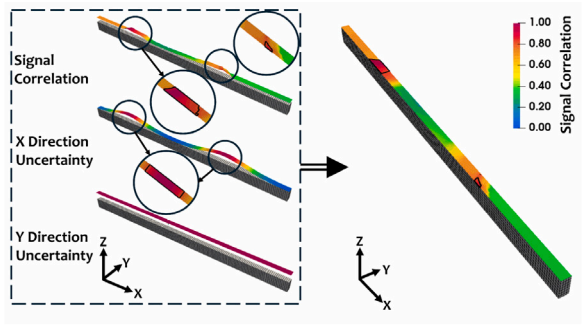


(b) Second ideal PS region

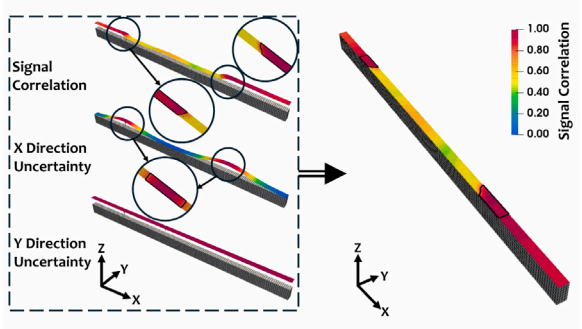


(c) Third ideal PS region

**Fig. 14.** Ideal PS regions for traffic loading failure.

positioning correction method. As an illustration example, we adopted the uncertainty values reported for the Sentinel and the single-epoch corner reflectors (CR) method [55]. In this case, the uncertainty in the $y$ direction (corresponding to the east–west orientation along the Marnixkade quay wall) was 3.47 m, while the uncertainty in the $x$ direction (north–south orientation) was 3.63 m. These uncertainties were modelled using an RBF kernel to account for spatial correlations. The results are shown in the "x direction uncertainty" and "y direction uncertainty" panels in Figs. 14(a)–14(c). Similar to the signal correlation, the positions with correlation values above 0.8 were considered acceptable alternatives to the top-selected position from a positional uncertainty perspective (highlighted by black outlines in each panel).

Finally, the region for each ideal PS was defined as the intersection of the regions meeting all three criteria: high signal correlation, acceptable $x$-direction uncertainty and acceptable $y$-direction uncertainty. The regions for first, second and third ideal PS are shown in the right panels of Figs. 14. It can be observed that the second and third ideal PSs exhibit an almost symmetric regional placement, reflecting the inherent symmetry of the structural damage mechanism.

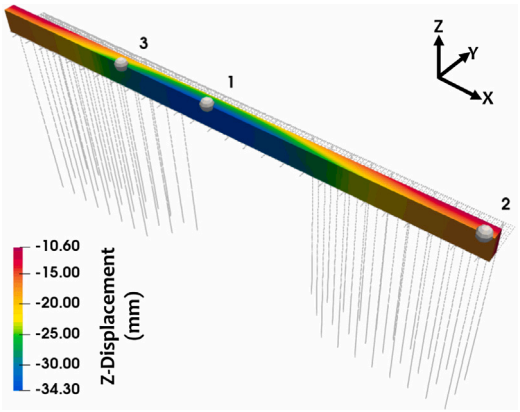


**Fig. 15.** Top selected ideal PSs and vertical displacements at the final load step for the central piles degradation case. All parts other than the masonry walls are shown in dashed lines.

### 4.2. Failure induced by degradation of central foundation piles

The second scenario was the failure induced by the degradation of central foundation piles. The failed piles were unevenly distributed across the three pile rows: 11 in the front (nearest the water), 9 in the middle row, and 7 in the back (see Fig. 10(a)). Since the degradation of the central foundation piles induced significantly larger displacements in the vertical direction ($z$ direction), compared to the other two directions, the vertical displacements were used as inputs for this analysis. Fig. 15 shows the vertical displacements at the final load step of the numerical simulations. The largest displacements were concentrated in the central region, where the degraded piles were located, with a maximum value of −34.3 mm. Due to the symmetric layout of the degraded piles along the $x$ direction, the displacement pattern also showed a symmetric distribution.

To evaluate surface representability, we compared the reconstruction errors between the pseudo sensor and virtual MT-InSAR. As shown in Fig. 16, the reconstruction error of virtual MT-InSAR was comparable to that of the pseudo sensor, suggesting that surface measurements alone are sufficient to capture the overall mechanism.

The top selected positions for the first three ideal PSs are shown in Fig. 15: the first ideal PS was located in the area with the maximum vertical displacement (in blue colour), corresponding to the centre of the degraded piles. The second ideal PS was positioned in a region that was less affected by the degradation, while the third was located near the boundary of the degraded pile region.

After applying the modified pivoted QR factorisation, the signal correlation over the selection sequence for each ideal PS is shown in Fig. 17. The significant variation in the correlation values for the first and second ideal PSs suggests that critical displacement characteristics continued to emerge (Fig. 17(a) and (b)). On the other hand, the

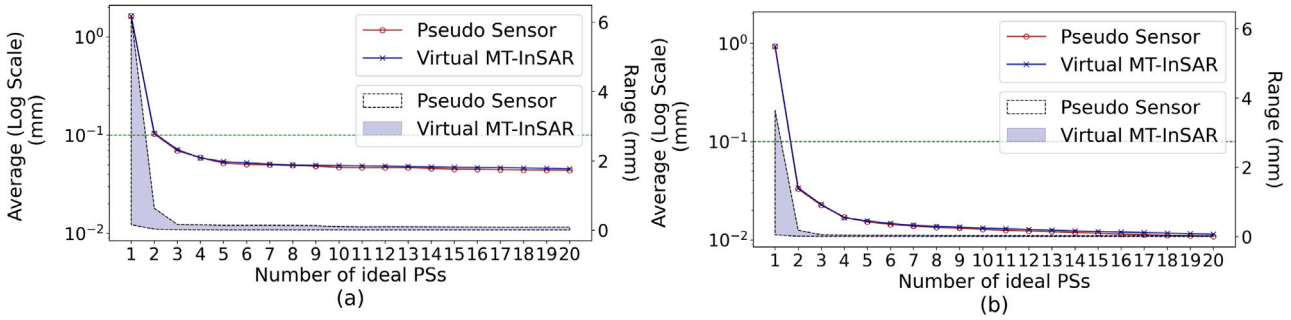


**Fig. 16.** Evaluation of the surface displacement capability to represent central piles degradation failure: (a) maximum absolute reconstruction error and (b) mean square absolute reconstruction error. The average reconstruction error is shown by lines, while the dashed envelopes and the shaded areas represent the corresponding error ranges.

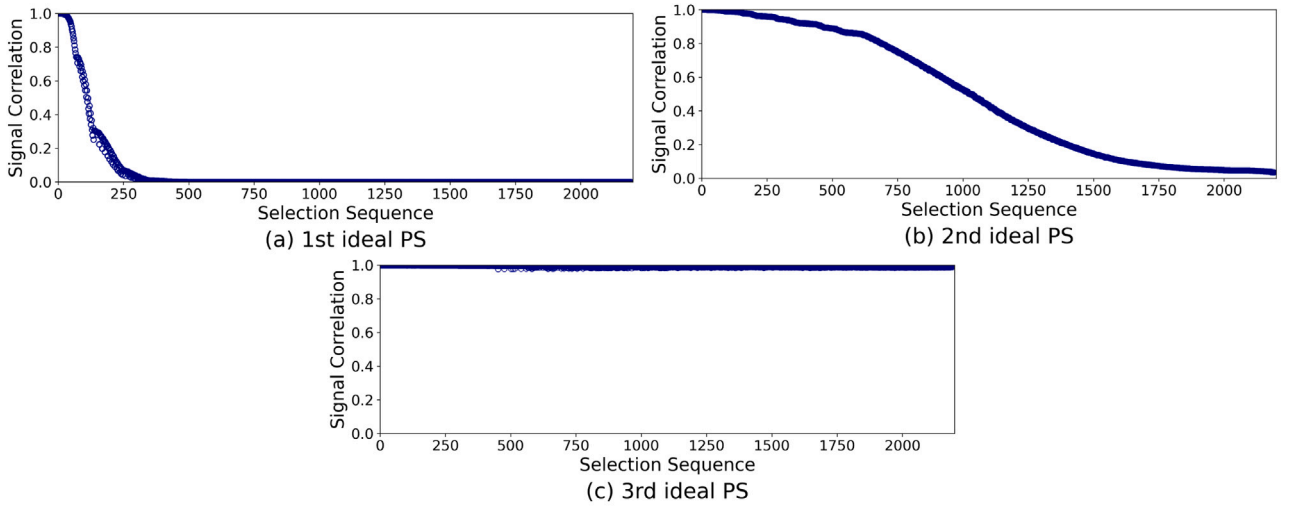


**Fig. 17.** Signal correlation trends during sequential selection for each ideal PS, in case of central pile degradation.

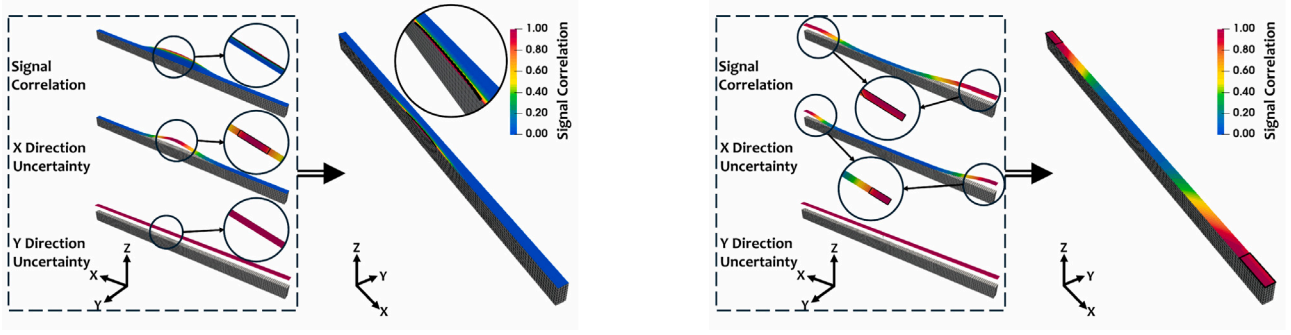


(a) First ideal PS region for central pile degradation

(b) Second ideal PS region for central pile degradation

**Fig. 18.** Ideal PS regions for central pile degradation failure.

consistently high correlation for the third ideal PS (Fig. 17(c)) indicates that its contribution was minimal, implying that its inclusion was not necessary.

As shown in the right panels of Figs. 18, the signal correlations for each ideal PS are displaced spatially on the top surface, along with the MT-InSAR's position uncertainties in both the $x$ and $y$ directions. The uncertainties in the $x$ and $y$ directions remained 3.63 m and 3.47 m, respectively, and were modelled using an RBF kernel. Locations where both the signal and spatial correlation values exceeded 0.8 were considered as the representative region for each ideal PS, as shown in the left panels. Like the previous case study, the failure induced by the degradation of central piles exhibited symmetric features, leading to two representative regions for the second ideal PS.

### 4.3. Failure induced by degradation of random foundation piles

Compared to previous case studies, assuming a random, non-localised failure of foundation piles better reflected real-world scenarios. This random distribution of damage at the foundation level resulted in a damage mechanism that produced a displacement pattern with greater asymmetry compared to the previously tested damage mechanisms. This mechanism primarily induced displacements in the vertical direction ($z$ direction), which were used as inputs for the

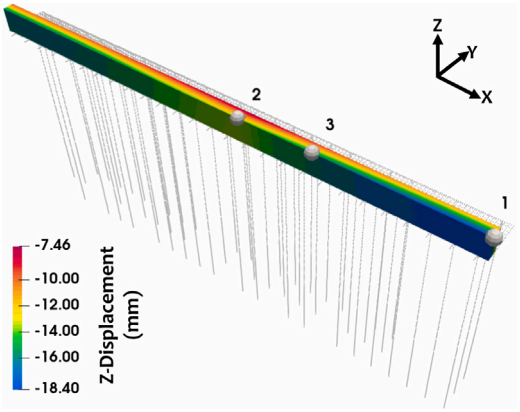


**Fig. 19.** Top selected ideal PSs and vertical displacements at the final load step for the random piles degradation case. All parts other than the masonry walls are shown in dashed lines.

analysis. Fig. 19 shows the vertical displacements at the final load step of the numerical simulations. The largest displacements were observed at the right edge of the quay wall (blue area), where most piles were degraded, with a maximum displacement of −18.4 mm. The surface displacement representability was validated by the results obtained after introducing a pseudo sensor, as shown in Fig. 20.

The top selected position for each ideal PS is shown in Fig. 19. The first ideal PS was located in the region with the highest concentration of failed piles, while the second ideal PS was placed where the pile degradation was least concentrated. The third was positioned in the intermediate region. Similar to previous cases, each ideal PS was processed by modified pivoted QR factorisation to identify the region. The correlation between the new selection and the top selection is illustrated in Fig. 21. Since the correlation for the second ideal PS (Fig. 21(b)) already ranged between 0.5 and 1, and the correlation for the third ideal PS (Fig. 21(c)) remained consistently at 1, the third ideal PS was unnecessary.

Subsequently, the obtained signal correlations were combined with the uncertainties in both the $x$ (3.63 m) and $y$ directions (3.47 m) to identify the ideal PS regions. The resulting regions are presented in the right panels of Figs. 22.

## 5. Translating case study findings to city-wide MT-InSAR evaluation in Amsterdam

Based on the simulations performed on the Marnixkade quay wall, the proposed method was used to identify ideal PS regions for detecting the three specific damage mechanisms described in the previous section. These regions can serve as benchmarks to evaluate the practical applicability of MT-InSAR at a regional scale. To this end, we conducted a systematic assessment to determine whether MT-InSAR can effectively detect these mechanisms across the quay walls of Amsterdam historic centre.

The historical centre of Amsterdam was selected as the test area due to its dense network of historic quay walls, most of which were constructed over a century ago and have remained in active use until today [63]. Fig. 23 shows the target area. Quay walls are marked in red, while real PSs collected between 2011 and 2020 from ascending and descending satellite tracks are overlaid. These PSs were derived from TerraSAR-X imagery and processed by SkyGeo using their proprietary PyAntares algorithm, which is based on the method proposed by Van Leijen [64]. A preliminary filtering was applied as a vertical measurement tolerance around the top surface of the quay walls. This tolerance was defined based on a correlation threshold of 0.8 to account for the uncertainty in the $z$ direction.

The Amsterdam Municipality reports that structural typology data is incomplete for all quay walls [65]. However, among the quay walls with available information, a total length of 10233.45 km has been documented. Of this, 7158.12 km, about 70%, share the same structural typology as the Marnixkade quay wall. This substantial proportion supports the use of the Marnixkade simulation as a representative model for quay walls in Amsterdam's historic centre.

The numerical model for Marnixkade had a length of 29.7 m, which was determined through sensitivity analysis assessing its impact on quay wall displacements [58]. However, the actual quay walls in Amsterdam historic centre are significantly longer. To ensure comprehensive coverage, each quay wall was divided into overlapping 29.7 m segments, with a 1 m sliding window between consecutive segments. This segmentation approach ensured that all parts of the quay walls were systematically analysed while keeping each segment length consistent with the numerical model.

The regional benchmarking involved a two-step analysis: first, the real PSs identified within each segment were assessed to determine whether they fell within the ideal PS regions for each structural mechanism. This step provided a binary result ("yes" or "no") for each ideal region and mechanism, indicating whether the real PSs aligned with the identified ideal regions. Second, the reconstruction error relative to the real PSs was calculated to provide a quantitative measure of MT-InSAR's effectiveness. The reconstruction error was calculated using the method described in previous sections, as shown in Eq. (9). While earlier sections focused on the reconstruction error of the identified ideal PSs, this evaluation extended the analysis to the real PSs present in the segments.

The results of evaluating MT-InSAR's effectiveness in Amsterdam historical centre show that for ascending geometry, 25.11% of the segments had at least one PS, while for descending geometry, this percentage was 24.2%. As illustrative examples, we considered failure induced by the degradation of central foundation piles and failure

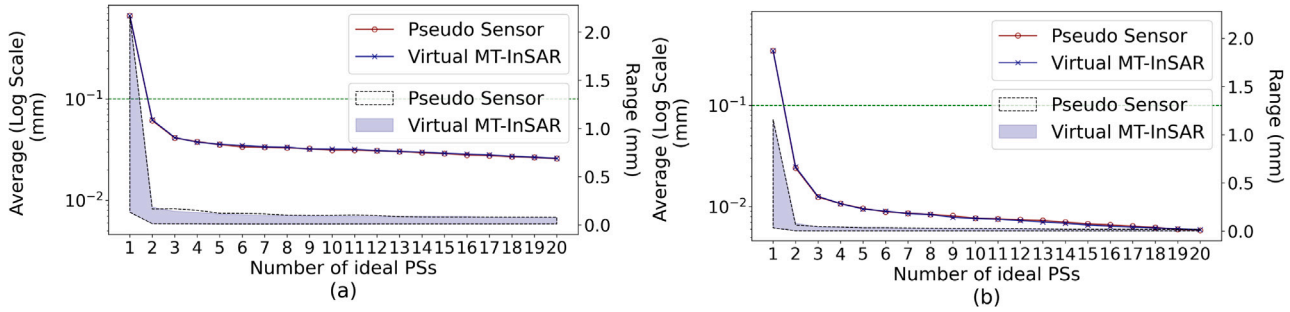


**Fig. 20.** Evaluation of the surface displacement capability to represent random piles degradation failure: (a) maximum absolute reconstruction error and (b) mean square absolute reconstruction error. The average reconstruction error is shown by lines, while the dashed envelopes and the shaded areas represent the corresponding error ranges.

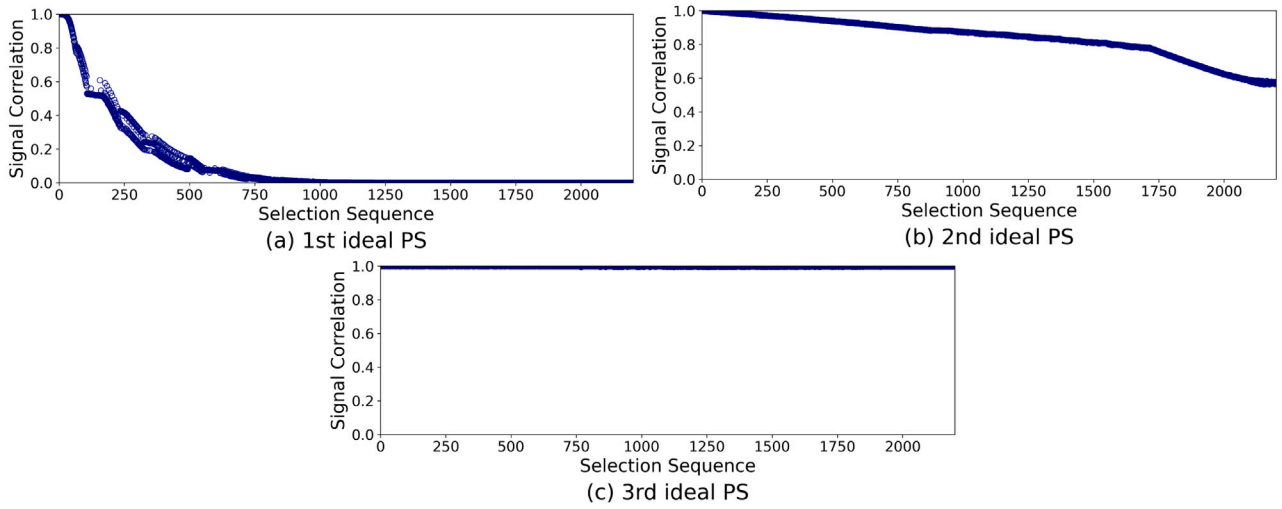


**Fig. 21.** Signal correlation trends during sequential selection for each ideal PS, in case of random piles degradation.

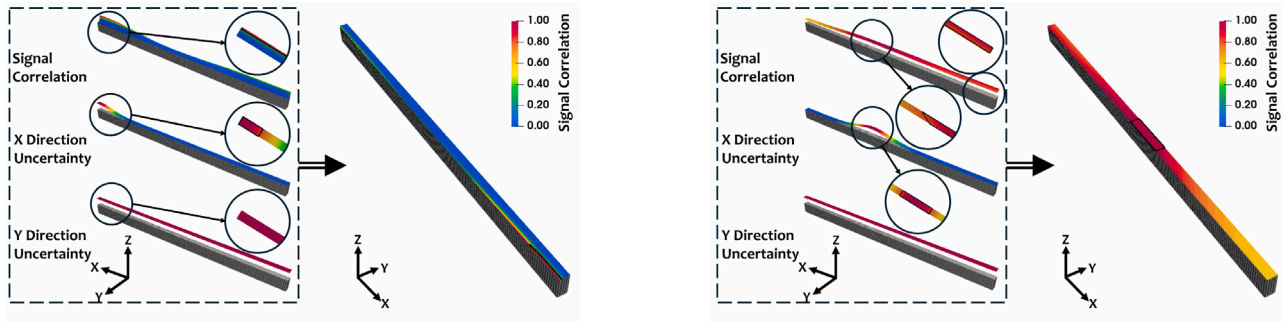


(a) First ideal PS region for random piles degradation

(b) Second ideal PS region for random piles degradation

**Fig. 22.** Ideal PS regions for random piles degradation failure.

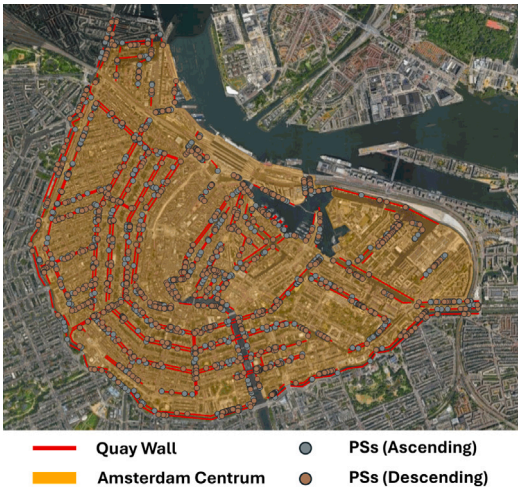


**Fig. 23.** Study area: Amsterdam historic centre with quay walls and PS data.

induced by traffic loading, using real PSs collected in ascending geometry. As shown in Fig. 18(a), the first ideal PS region for the failure induced by the degradation of central foundation piles was relatively small. Consequently, segments with real PSs in this region were rare, as illustrated in Fig. 24(a) . This scarcity of PSs resulted in large reconstruction errors, as shown in Fig. 24(c) and Fig. 24(d). In contrast, for the failure induced by traffic loading, many segments contained real PSs in the first, second and third ideal PS regions, as shown in Fig. 25(a) to 25(c). This led to lower reconstruction errors for most segments, as depicted in Figs. 25(d) and 25(e). Comparing these two mechanisms, MT-InSAR demonstrated a greater monitoring ability for traffic loading failure, as more segments of the quay wall can be effectively observed.

Other results can be found in Appendix A. These results demonstrate that the ideal PS regions identified through the proposed approach can help determine which parts of the quay walls are detectable by MT-InSAR for specific damage mechanisms.

## 6. Discussion

The results demonstrate that the proposed method can effectively identify ideal PSs, which serve as benchmarks to assess the spatial adequacy of real PS distributions obtained from MT-InSAR data. By comparing the locations of real PSs with the ideal PS regions, the practical applicability of MT-InSAR for SHM can be evaluated. When real PSs are located within the ideal PS regions, it indicates that MT-InSAR is well-positioned to detect critical displacement patterns associated with structural damage mechanisms. In such cases, the monitoring data is considered reliable for capturing the relevant structural response, and MT-InSAR can be confidently used as a tool for damage detection. It is worth mentioning that depending on the infrastructure under


(a) Segments with PSs in 1st ideal region (b) Segments with PSs in 2nd ideal region

(c) Mean square absolute reconstruction error (mm) (d) Maximum absolute reconstruction error (mm)

**Fig. 24.** MT-InSAR's effectiveness in detecting the failure induced by degradation of central foundation piles in the historical centre of Amsterdam (ascending geometry)


(a) Segments with PSs in 1st ideal region (b) Segments with PSs in 2nd ideal region (c) Segments with PSs in 3rd ideal region

(d) Mean square absolute reconstruction error (mm) (e) Maximum absolute reconstruction error (mm)

**Fig. 25.** MT-InSAR's effectiveness in detecting the failure induced by traffic loading in the historical centre of Amsterdam (ascending geometry)

investigation, it might occur that real PSs are absent from the ideal PS regions. Consequently, the effectiveness of MT-InSAR in detecting the damage mechanism would become limited. The absence of real PSs may result from various factors such as the satellite's acquisition geometry, unfavourable viewing angles, or obstructions like vegetation or urban structures that block the line of sight. Issues related to real PS availability, including visibility analysis, layover, and shadowing, have been discussed in previous works [26]. In these situations, MT-InSAR could be used in combination with other complementary damage detection techniques, such as ground-based sensors, or alternative remote sensing methods, to ensure comprehensive and reliable SHM.

Compared to conventional metrics based solely on PS density, the proposed method significantly enhances the assessment framework by incorporating both temporal and spatial characteristics from numerically simulating potential structural damage mechanisms. This integration not only improves the accuracy of evaluating MT-InSAR's performance but also supports the development of more robust damage indicators. Most existing MT-InSAR-based damage detection approaches are trend-based, focusing on temporal anomalies such as unexpected acceleration or cumulative displacements at PS locations. By considering spatial relationships between PSs and their relevance to specific damage mechanisms, the proposed method enables a shift to more predictive and structurally informed monitoring strategies. Furthermore, since the proposed method relies exclusively on displacement data as input, it is not limited to any particular structural typology. Provided that suitable methods are used to obtain representative displacement measurements, the framework can be applied directly to a wide variety of structures, making it highly adaptable and widely applicable.

While this method represents significant advancement, it also raises a few practical considerations. One of these concerns the choice of reconstruction strategy. During the surface representation evaluation, a linear mapping approach was employed to estimate the reconstruction error. Its performance was benchmarked against a nonlinear method, the Kernel Ridge Regression (KRR) [66]. In this case both approaches achieved comparable accuracy, with KRR requiring a substantially higher computational effort due to hyperparameter tuning (see Appendix B for more details). Given this trade-off between accuracy and efficiency, the linear mapping approach was adopted for the present case study. For applications involving more complex structures, such comparisons might be revisited, as different geometries or data characteristics could influence which reconstruction technique is most suitable.

Computational requirements should be considered when applying the proposed method. These requirements arise mainly from three component: numerical modelling, displacement matrix size, and structure segmentation. FEA has long been an established standard for structural analysis [67]. However, high-fidelity finite element analysis (FEA) can be computationally demanding, particularly for large or complex structures. Variations in key parameters like foundation stiffness, pile spacing, or wall thickness could potentially alter deformation modes and ideal PS locations. High-fidelity FE models are typically developed and validated when dealing with critical infrastructures, and it is assumed that this was available in the present study (as detailed in Section 5). FE model-based sensitivity study and appropriate uncertainty quantification strategies might be required to quantify how much the identified ideal PS regions shift when these parameters are varied within realistic bounds for historic quay walls. Alternatively, when no validated FE model is available, alternative models such as surrogate or analytical models can be employed. Since the proposed method relies only on displacement outputs rather than element-level formulations, these alternatives provide a practical and cost-effective means of generating the required data without limiting the applicability of the approach.

The size of the displacement matrix can influence computational cost and accuracy, especially for large structures. In the preliminary analysis of the case study, we compared the identification of ideal PSs using the full displacement matrix with that obtained from a dimensionally reduced matrix derived from POD. The results indicated that full displacement matrix provided a satisfactory balance between computational cost and accuracy. For other structures, similar assessments may be useful to determine an efficient and reliable basis matrix.

Finally, in the present case study, the considerable length of the quay walls and the limited information on their possible subdivision made it necessary to apply segmentation through a sliding window, which introduced additional computational cost. This requirement, however, is not universal. For shorter structures, such as bridges, segmentation may be minimal or unnecessary. Even for long structures, incorporating prior information, such as the presence of expansion joints, can reduce the number of required segments, thereby lowering computational cost.

## 7. Conclusions

This study introduced a novel structural-based inverse approach for systematically assessing the effectiveness of MT-InSAR for SHM. The proposed approach integrates structural behaviour characteristics with MT-InSAR measurement properties, moving beyond traditional assessments based solely on PS density and enabling a more reliable evaluation of MT-InSAR applicability for different structural damage mechanisms.

First, a numerical simulation of potential structural damage mechanisms was conducted to generate displacement data, which were then analysed to assess whether surface-only measurements, typical of MT-InSAR observations, can reliably represent the internal structural behaviour. Second, when surface displacements were found to be representative, the concept of "ideal PSs" was introduced. These identified ideal PSs served as benchmarks to assess the adequacy of real PS distributions obtained from actual MT-InSAR satellite observations.

The applicability and robustness of the proposed approach were demonstrated through a practical case study involving the Marnixkade quay wall in Amsterdam. The results validated the capability of the proposed method to effectively evaluate whether surface displacement measurements could capture the entire structural responses and to accurately determine the ideal PSs. These ideal PSs were subsequently applied as benchmarks for evaluating the effectiveness of MT-InSAR in detecting quay walls across the whole Amsterdam historical centre. This city-scale implementation demonstrated the practical utility of the approach in operational SHM scenarios.

In conclusion, the proposed approach provides a structured, robust and scalable framework for evaluating MT-InSAR's applicability in SHM. It explicitly integrates structural behaviour, damage mechanism characteristics, and MT-InSAR measurement constraints, thereby advancing the practical adoption of satellite-based monitoring technologies.

## CRediT authorship contribution statement

**Hao Kuai:** Writing – original draft, Visualization, Validation, Software, Methodology, Formal analysis, Conceptualization. **Valentina Macchiarulo:** Writing – review & editing, Validation, Software, Formal analysis, Conceptualization. **Satyadhrik Sharma:** Writing – review & editing, Software, Data curation. **Pantelis Karamitopoulos:** Writing – review & editing, Data curation. **Francesco Messali:** Writing – review & editing, Supervision. **Alice Cicirello:** Writing – review & editing, Supervision, Methodology. **Giorgia Giardina:** Writing – review & editing, Validation, Supervision, Project administration, Funding acquisition, Conceptualization.

## Funding

This work is part of the Vidi project InStruct, project number 18912, financed by the Dutch Research Council (NWO).

## Declaration of competing interest

The authors declare the following financial interests/personal relationships which may be considered as potential competing interests: Giorgia Giardina reports financial support was provided by Dutch Research Council. If there are other authors, they declare that they have no known competing financial interests or personal relationships that could have appeared to influence the work reported in this paper.

## Acknowledgments

The authors acknowledge SkyGeo Netherlands B.V. for providing InSAR data.

## Appendix A. MT-InSAR's effectiveness in the historical centre of Amsterdam

See Tables A.1–A.3

**Table A.1**
MT-InSAR's capability of detecting failure induced by traffic load of quay walls in the historic centre of Amsterdam.

| Description | Ascending | Descending |
|---|---|---|
| Segments with PSs in the 1st ideal region |  |  |
| Segments with PSs in the 2nd ideal region |  |  |
| Segments with PSs in the 3rd ideal region |  |  |
| Mean square absolute reconstruction error (mm) | 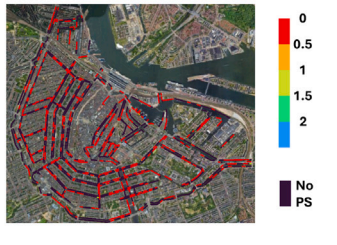 | 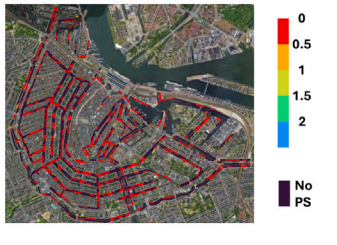 |
| Maximum absolute reconstruction error (mm) | 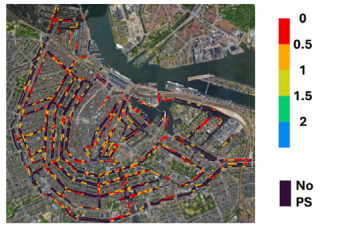 | 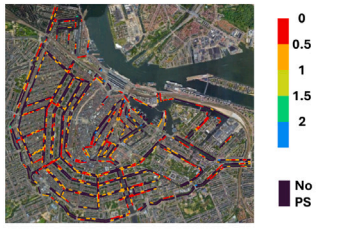 |

**Table A.2**
MT-InSAR's capability of detecting failure induced by degradation of central foundation piles of quay walls in the historic centre of Amsterdam.

| Description | Ascending | Descending |
|---|---|---|
| Segments with PSs in 1st ideal region |  |  |
| Segments with PSs in 2nd ideal region |  | 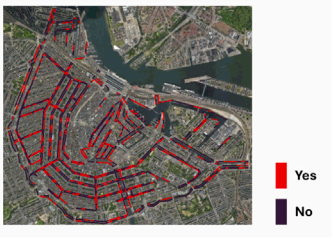 |
| Mean square absolute reconstruction error (mm) | 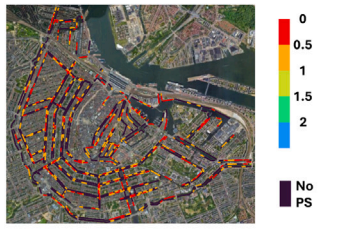 | 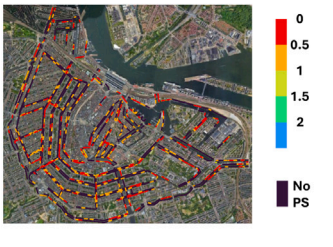 |
| Maximum absolute reconstruction error (mm) | 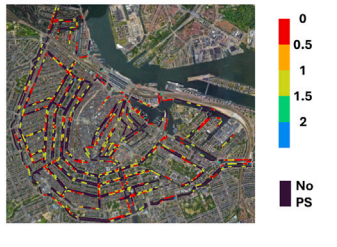 | 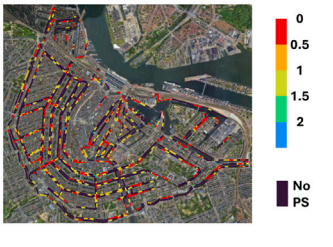 |

**Table A.3**
MT-InSAR's capability of detecting failure induced by degradation of random foundation piles of quay walls in the historic centre of Amsterdam.

| Description | Ascending | Descending |
|---|---|---|
| Segments with PSs in the 1st ideal region |   |   |
| Segments with PSs in the 2nd ideal region |   | 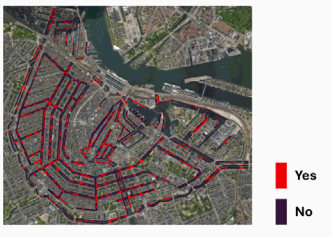  |
| Mean square absolute reconstruction error (mm) | 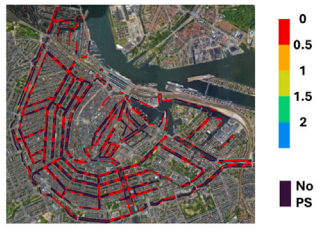  | 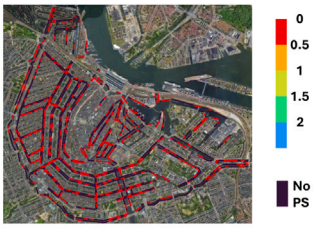  |
| Maximum absolute reconstruction error (mm) | 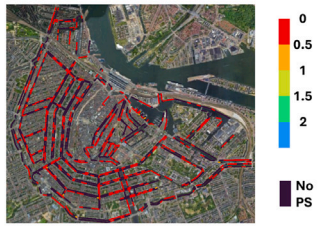  | 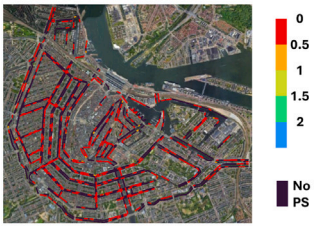  |

## Appendix B. Comparison between linear and nonlinear mapping

To examine whether the linear mapping used for evaluating reconstruction error is sufficient given the potentially nonlinear nature of structural degradation, we conducted a quantitative comparison with a nonlinear regression method, namely Kernel Ridge Regression (KRR) [66].

KRR performs nonlinear regression by implicitly mapping the input data into a high-dimensional feature space using a kernel function and subsequently fitting a regularised linear model in that space. The model involves two key hyper-parameters: the regularisation parameter, which controls the model complexity, and the kernel coefficient, which determines the influence radius of the data points, where larger values result in more localised influence.

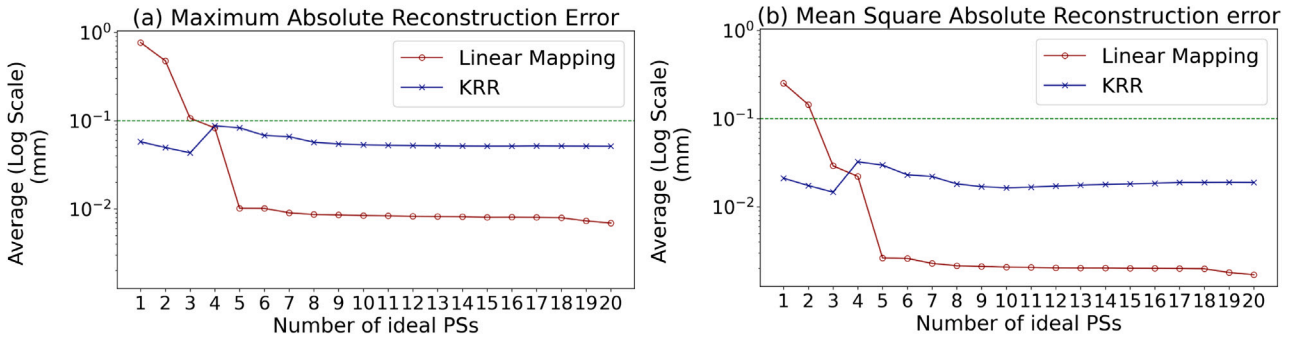


**Fig. B.1.** The reconstruction error using linear mapping and KRR considering different number of ideal PSs: (a) the maximum absolute reconstruction error and (b) the mean square absolute reconstruction error.

To ensure solution robustness and identify the performance, we conducted a 5-fold cross-validation to determine the best combination of $\alpha$ and $\gamma$ for KRR.

As a representative case, the failure induced by traffic loading was used for evaluation. Fig. B.1 presents the reconstruction errors obtained from both linear mapping and KRR under varying number of ideal PSs. The results indicate that KRR achieves lower reconstruction errors when the number of ideal PSs is small, demonstrating its stronger capability for modelling nonlinear relationships. However, as the number of PSs increases, the reconstruction error of the linear mapping method converges rapidly to the sub-millimetre scale, which is sufficiently small for practical SHM applications.

In terms of computational efficiency, the linear mapping approach required only 2.5075 s, whereas KRR (including hyperparameter tuning via cross-validation) required 47.9340 s. These experiments were conducted on a laptop equipped with a 12th-generation intel i7-1265U CPU and 16 GB RAM. Thus, KRR is approximately 19 times more computationally expensive than the linear mapping method.

Considering both the reconstruction accuracy and computational cost, this comparative analysis demonstrates that the linear mapping method provides a highly efficient and sufficiently accurate solution for the studied case.

## Data availability

Non commercial data can be made available on request.

## References


[1] Ellingwood Bruce R. Risk-informed Condition Assessment of Civil Infrastructure: State of Practice and Research Issues. Struct Infrastruct Eng 2005;1(1):7–18.

[2] Jensen Jens, Casas Joan, Karoumi Raid, Plos Mario, Cremona Christian, Melbourne Clive. Guideline for load and resistance assessment of existing European railway bridges. Technical report, 2008.

[3] Aktan AE, Brownjohn JMW. Structural Identification: Opportunities and Challenges. J Struct Eng 2013;139(10):1639–47.

[4] Mori Yasuhiro, Ellingwood Bruce R. Reliability-Based Service-Life Assessment of Aging Concrete Structures. J Struct Eng 1993;119(5):1600–21.

[5] Kumar Prashant, Imam Boulent. Footprints of Air Pollution and Changing Environment on the Sustainability of Built Infrastructure. Sci Total Environ 2013;444:85–101.

[6] Chen Huapeng, Ni Yiqing. Introduction to structural health monitoring. In: Structural health monitoring of large civil engineering structures, chapter 1. John Wiley & Sons, Ltd; 2018, p. 1–14.

[7] Shim Seungbo. Self-training approach for crack detection using synthesized crack images based on conditional generative adversarial network. Computer-Aided Civ Infrastruct Eng 2023;39(7):1019–41.

[8] American Association of State Highway and Transportation Officials. The Manual for Bridge Evaluation, . In: American association of state highway and transportation officials. Washington, D.C., 2nd ed. /2011 edition. 2011.

[9] Federal Highway Administration USA. National bridge inspection standards. 2022.

[10] Ministry of Transport of the People's Republic of China. Standards for technical condition evaluation of highway bridges. 2011.

[11] Ministry of Infrastructure and Sustainable Mobility. 2022, Guidelines for Risk Classification and Management, Safety Assessment, and Monitoring of Existing Bridges.

[12] German Institute for Standardization. Engineering structures along roads and paths – monitoring and inspection. 2024.

[13] Le Tuan, Gibb Spencer, Pham Nhan, La Hung Manh, Falk Logan, Berendsen Tony. Autonomous Robotic System Using Non-destructive Evaluation Methods for bridge deck inspection. In: 2017 IEEE international conference on robotics and automation (ICRA). 2017, p. 3672–7.

[14] Feroz Sainab, Dabous Saleh Abu. UAV-Based Remote Sensing Applications for Bridge Condition Assessment. Remote Sens 2021;13(9):1809.

[15] Washer Glenn, Connor Robert, Nasrollahi Massoud, Provines Jason. New Framework for Risk-Based Inspection of Highway Bridges. J Bridg Eng 2016;21(4):04015077.

[16] Ferretti A, Prati C, Rocca F. Nonlinear subsidence rate estimation using permanent scatterers in differential SAR interferometry. IEEE Trans Geosci Remote Sens 2000;38(5):2202–12.

[17] Ferretti A, Prati C, Rocca F. Permanent Scatterers in SAR interferometry. IEEE Trans Geosci Remote Sens 2001;39(1):8–20.

[18] Ferretti Alessandro, Savio Giuliano, Barzaghi Riccardo, Borghi Alessandra, Musazzi Sergio, Novali Fabrizio, Prati Claudio, Rocca Fabio. Submillimeter Accuracy of InSAR Time Series: Experimental Validation. IEEE Trans Geosci Remote Sens 2007;45(5):1142–53.

[19] Rucci A, Ferretti A, Monti Guarnieri A, Rocca F. Sentinel 1 SAR interferometry applications: The outlook for sub millimeter measurements. Remote Sens Environ 2012;120:156–63.

[20] Selvakumaran Sivasakthy, Plank Simon, Geib Christian, Rossi Cristian, Middleton Campbell. Remote monitoring to predict bridge scour failure using Interferometric Synthetic Aperture Radar (InSAR) stacking techniques. Int J Appl Earth Obs Geoinf 2018;73:463–70.

[21] Milillo Pietro, Giardina Giorgia, Perissin Daniele, Milillo Giovanni, Coletta Alessandro, Terranova Carlo. Pre-Collapse Space Geodetic Observations of Critical Infrastructure: The Morandi Bridge, Genoa, Italy. Remote Sens 2019;11(12):1403.

[22] Farneti Elisabetta, Cavalagli Nicola, Costantini Mario, Trillo Francesco, Minati Federico, Venanzi Ilaria, Ubertini Filippo. A method for structural monitoring of multispan bridges using satellite InSAR data with uncertainty quantification and its pre-collapse application to the Albiano-Magra Bridge in Italy. Struct Health Monit 2023;22(1):353–71.

[23] Macchiarulo Valentina, Kuai Hao, Karamitopoulos Pantelis, Milillo Pietro, Giardina Giorgia. Structural evaluation of urban bridges in Amsterdam through InSAR-based displacement data. E-Journal Nondestruct Test 29(07):2024.

[24] Perissin Daniele, Wang Zhiying, Lin Hui. Shanghai subway tunnels and highways monitoring through Cosmo-SkyMed Persistent Scatterers. ISPRS J Photogramm Remote Sens 2012;73:58–67.

[25] Giardina Giorgia, Milillo Pietro, DeJong Matthew J, Perissin Daniele, Milillo Giovanni. Evaluation of InSAR monitoring data for post-tunnelling settlement damage assessment. Struct Control Health Monit 2019;26(2):e2285.

[26] Macchiarulo Valentina, Milillo Pietro, DeJong Matthew J, Martí Javier González, Sánchez Jordi, Giardina Giorgia. Integrated InSAR monitoring and structural assessment of tunnelling-induced building deformations. Struct Control Health Monit 2021;28(9):e2781.

[27] Drougkas Anastasios, Verstrynge Els, Balen Koenraad Van, Shimoni Michal, Croonenborghs Thibauld, Hayen Roald, Declercq Pierre-Yves. Country-scale InSAR monitoring for settlement and uplift damage calculation in architectural heritage structures. Struct Health Monit 2021;20(5):2317–36.

[28] Carlo Fabio Di, Miano Andrea, Giannetti Ilaria, Mele Annalisa, Bonano Manuela, Lanari Riccardo, Meda Alberto, Prota Andrea. On the integration of multi-temporal synthetic aperture radar interferometry products and historical surveys data for buildings structural monitoring. J Civ Struct Health Monit 2021;11(5):1429–47.

[29] Ma Peifeng, Zheng Yi, Zhang Zhengjia, Wu Zherong, Yu Chang. Building risk monitoring and prediction using integrated multi-temporal InSAR and numerical modeling techniques. Int J Appl Earth Obs Geoinf 2022;114:103076.

[30] Mazzanti P, Perissin D, Rocca A. Structural Health Monitoring of Dams by Advanced Satellite SAR Interferometry: Investigation of Past Processes and future monitoring perspectives. In: 7th international conference on structural health monitoring of intelligent infrastructure (SHMII 2015). Torino, 2015.

[31] Marchamalo-Sacristán Miguel, Ruiz-Armenteros Antonio Miguel, Lamas-Fernández Francisco, González-Rodrigo Beatriz, Martínez-Marín Rubén, Delgado-Blasco José Manuel, Bakon Matus, Lazecky Milan, Perissin Daniele, Papco Juraj, Sousa Joaquim J. MT-InSAR and Dam Modeling for the Comprehensive Monitoring of an Earth-Fill Dam: The Case of the Benínar Dam (Almería, Spain). Remote Sens 2023;15(11):2802.

[32] Tavakkoliestahbanati Amin, Milillo Pietro, Kuai Hao, Giardina Giorgia. Pre-collapse Spaceborne Deformation Monitoring of the Kakhovka dam. Ukr, from 2017 To 2023. Commun Earth & Environ 2024;5(1):1–9.

[33] Qin Xiaoqiong, Liao Mingsheng, Zhang Lu, Yang Mengshi. Structural Health and Stability Assessment of High-Speed Railways via Thermal Dilation Mapping With Time-Series InSAR Analysis. IEEE J Sel Top Appl Earth Obs Remote Sens 2017;10(6):2999–3010.

[34] Chang Ling, Dollevoet Rolf PBJ, Hanssen Ramon F. Nationwide Railway Monitoring Using Satellite SAR Interferometry. IEEE J Sel Top Appl Earth Obs Remote Sens 2017;10(2):596–604.

[35] D'Amico Fabrizio, Gagliardi Valerio, Ciampoli Luca Bianchini, Tosti Fabio. Integration of InSAR and GPR techniques for monitoring transition areas in railway bridges. NDT & E Int 2020;115:102291.

[36] Chen Mi, Li Zhenhong, Tomás Roberto, Herrera Gerardo, Gong Huili, Li Xiaojuan, Gao Wenfeng, Hu Leyin. Land subsidence-induced damage assessment along Beijing–Tianjin high-speed railway from space using high-resolution TerraSAR-X data. Struct Health Monit 2025. 14759217251334328.

[37] Sousa JJ, Bastos L. Multi-temporal SAR interferometry reveals acceleration of bridge sinking before collapse. Nat Hazards Earth Syst Sci 2013;13(3):659–67.

[38] Hanssen Ramon F. Satellite radar interferometry for deformation monitoring: A priori assessment of feasibility and accuracy. Int J Appl Earth Obs Geoinf 2005;6(3):253–60.

[39] Crosetto Michele, Monserrat Oriol, Cuevas-González María, Devanthéry Núria, Crippa Bruno. Persistent Scatterer Interferometry: A review. ISPRS J Photogramm Remote Sens 2016;115:78–89.
[40] Macchiarulo Valentina, Milillo Pietro, Blenkinsopp Chris, Reale Cormac, Giardina Giorgia. Multi-Temporal InSAR for Transport Infrastructure Monitoring: Recent Trends and Challenges. Proc Inst Civ Eng - Bridg Eng 2023;176(2):92–117.
[41] Milillo Pietro, Giardina Giorgia, DeJong Matthew, Perissin Daniele, Milillo Giovanni. Multi-Temporal InSAR Structural Damage Assessment: The London Crossrail Case Study. Remote Sens 2018;10(2):287.
[42] Zhu Mao, Wan Xiaoli, Fei Bigang, Qiao Zhuping, Ge Chunqing, Minati Federico, Vecchioli Francesco, Li Jiping, Costantini Mario. Detection of Building and Infrastructure Instabilities by Automatic Spatiotemporal Analysis of Satellite SAR Interferometry Measurements. Remote Sens 2018;10(11):1816.
[43] Chang Ling, Sakpal Nikhil P, Elberink Sander Oude, Wang Haoyu. Railway Infrastructure Classification and Instability Identification Using Sentinel-1 SAR and Laser Scanning Data. Sensors 2020;20(24):7108.
[44] Gagliardi Valerio, Tosti Fabio, Ciampoli Luca Bianchini, D'Amico Fabrizio, Alani Amir M, Battagliere Maria Libera, Benedetto Andrea. Monitoring of bridges by MT-InSAR and unsupervised machine learning clustering techniques. In: Earth resources and environmental remote sensing/GIS applications XII. vol. 11863, 2021, p. 132–40, SPIE.
[45] Gao Q, Crosetto M, Monserrat O, Palama R, Barra A. Infrastructure Monitoring Using the Interferometric Synthetic Aperture Radar (InSAR) Technique. In: The international archives of the photogrammetry, remote sensing and spatial information sciences, XLIII-b3-2022. 2022, p. 271–6.
[46] Ma Peifeng, Lin Hui, Wang Weixi, Yu Hanwen, Chen Fulong, Jiang Liming, Zhou Lifan, Zhang Zhengjia, Shi Guoqiang, Wang Jili. Toward Fine Surveillance: A review of multitemporal interferometric synthetic aperture radar for infrastructure health monitoring. IEEE Geosci Remote Sens Mag 2022;10(1):207–30.
[47] Businger Peter, Golub Gene H. Linear Least Squares Solutions by Householder Transformations. Numer Math 1965;7(3):269–76.
[48] Manohar Krithika, Brunton Bingni W, Nathan Kutz J, Brunton Steven L. Data-Driven Sparse Sensor Placement for Reconstruction: Demonstrating the Benefits of Exploiting Known Patterns. IEEE Control Syst Mag 2018;38(3):63–86.
[49] Zhang Qiannan, Wu Huafeng, Mei Xiaojun, Han Dezhi, Marino Mario Donato, Li Kuan-Ching, Guo Song. A Sparse Sensor Placement Strategy Based on Information Entropy and Data Reconstruction for Ocean Monitoring. IEEE Internet Things J 2023;10(22):19681–94.
[50] Gernhardt Stefan, Auer Stefan, Eder Konrad. Persistent scatterers at building facades – Evaluation of appearance and localization accuracy. ISPRS J Photogramm Remote Sens 2015;100:92–105.
[51] Dheenathayalan Prabu, Small David, Schubert Adrian, Hanssen Ramon F. High-precision Positioning of Radar Scatterers. J Geod 2016;90(5):403–22.
[52] Cundall PA, Strack ODL. A discrete numerical model for granular assemblies. Geotechnique 1979;29(1):47–65.
[53] Liang YC, Lee HP, Lim SP, Lin WZ, Lee KH, Wu CG. Proper orthogonal decomposition and its applications—part i: theory. J Sound Vib 2002;252(3):527–44.
[54] Penrose R. A generalized inverse for matrices. In: Mathematical proceedings of the cambridge philosophical society. vol. 51, (3):1955, p. 406–13.
[55] Yang Mengshi, López-Dekker Paco, Dheenathayalan Prabu, Liao Mingsheng, Hanssen Ramon F. On the value of corner reflectors and surface models in InSAR precise point positioning. ISPRS J Photogramm Remote Sens 2019;158:113–22.
[56] Pedregosa Fabian, Varoquaux Gaël, Gramfort Alexandre, Michel Vincent, Thirion Bertrand, Grisel Olivier, Blondel Mathieu, Müller Andreas, Nothman Joel, Louppe Gilles, Prettenhofer Peter, Weiss Ron, Dubourg Vincent, Vanderplas Jake, Passos Alexandre, Cournapeau David, Brucher Matthieu, Perrot Matthieu, Duchesnay Édouard. Scikit-learn: Machine Learning in Python. 2018.
[57] van Leijen FJ, Ketelaar VBH, Marinkovic PS, Hanssen RF. Persistent scatterer interferometry: precision, reliability and integration. In: Proceedings of ISPRS hannover workshop. 2005.
[58] Sharma Satyadhrik, Longo Michele, Messali Francesco. A novel tier-based numerical analysis procedure for the structural assessment of masonry quay walls under traffic loads. Front Built Environ 2023;9.
[59] Sharma Satyadhrik, Longo Michele, Messali Francesco. Analysis procedures accounting for load redistribution mechanisms in masonry earth retaining structures under traffic loading. Eng Struct 2024;315:118420.
[60] Giordano Pier Francesco, Kamariotis Antonios, Giardina Giorgia, Chatzi Eleni, Limongelli Maria Pina. Uncertainty propagation in satellite InSAR data analysis for structural health monitoring. Autom Constr 2025;177:106371.
[61] Kamariotis Antonios, Vlachas Konstantinos, Ntertimanis Vasileios, Koune Ioannis, Cicirello Alice, Chatzi Eleni. On the Consistent Classification and Treatment of Uncertainties in structural health monitoring applications. ASCE-ASME J Risk Uncert Engrg Sys Part B Mech Engrg 2024;11(011108).
[62] Nebest BV. Marnixkade in Amsterdam. Funderingsonderzoek. definitive. Technical Report 2785401-01, Netherlands: Vianen, 2016.
[63] Luongo Davide, Nicodemo Gianfranco, Venmans Arjan, Korff Mandy, Sartorelli Luca, Maljaars Hanno, Peduto Dario. The Quay Walls of Amsterdam, Netherlands: An Approach for Collapse Risk Mitigation at the Municipal Scale Based on Multisource Monitoring and Surveying Data. J Geotech Geoenvironmental Eng 2025;151(2):05024014.
[64] Van Leijen FJ. Persistent Scatterer Interferometry Based on Geodetic Estimation Theory. Delft, (Ph.D. thesis), Delft University of Technology; 2014.
[65] ARK. Amsterdamse risicobeoordeling kademuren, versie 2.0. 2024, https://openresearch.amsterdam/nl/page/110353/ark-amsterdamse-risicobeoordeling-kademuren-versie-2.0.
[66] Regression Vladimir Vovk Kernel Ridge. Kernel ridge regression. In: Scholkopf Bernhard, Luo Zhiyuan, Vovk Vladimir, editors. Empirical inference: festschrift in honor of vladimir n,vapnik. Berlin, Heidelberg, Springer; 2013, p. 105–16.
[67] Liu Wing Kam, Li Shaofan, Park Harold S. Eighty Years of the Finite Element Method: Birth, Evolution, and future. Arch Comput Methods Eng 2022;29(6):4431–53.